Nuclear Physics B 367 (1991) 511–574
North-Holland

NUCLEAR
PHYSICS B

Determination of Z^0 resonance parameters and couplings from its hadronic and leptonic decays

DELPHI Collaboration

P. Abreu [a], W. Adam [b], F. Adami [c], T. Adye [d], T. Akesson [e], G.D. Alekseev [f], P. Allen, [g], S. Almehed [e], F. Alted [g], S.J. Alvsvaag [h], U. Amaldi [i], E. Anassontzis [j], P. Antilogus [k], W.-D. Apel [l], R.J. Apsimon [d], B. Åsman [m], P. Astier [n], J.-E. Augustin [o], A. Augustinus [i], P. Baillon [i], P. Bambade [o], F. Barao [a], G. Barbiellini [p], D.Y. Bardin [f], A. Baroncelli [q], O. Barring [e], W. Bartl [b], M. Battaglia [r], M.J. Bates [s], M. Baubillier [n], K.-H. Becks [t], C.J. Beeston [s], M. Begalli [u], P. Beilliere [v], Yu. Belokopytov [w], P. Beltran [x], D. Benedic [y], J.M. Benlloch [g], M. Berggren [m], D. Bertrand [z], S. Biagi [aa], F. Bianchi [ab], J.H. Bibby [s], M.S. Bilenky [f], P. Billoir [n], J. Bjarne [e], D. Bloch [y], S. Blyth [s], P.N. Bogolubov [f], T. Bolognese [c], M. Bonapart [ac], M. Bonesini [r], W. Bonivento [r], P.S.L. Booth [aa], M. Boratav [n], P. Borgeaud [c], G. Borisov [w], H. Borner [s], C. Bosio [q], O. Botner [ad], B. Bouquet [o], M. Bozzo [u], S. Braibant [i], P. Branchini [q], K.D. Brand [ae], R.A. Brenner [af], C. Bricman [z], R.C.A. Brown [i], N. Brummer [ac], J.-M. Brunet [v], L. Bugge [ag], T. Buran [ag], H. Burmeister [i], J.A.M.A. Buytaert [z], M. Caccia [i], M. Calvi [r], A.J. Camacho Rozas [ah], J.-E. Campagne [i], A. Campion [aa], T. Camporesi [i], V. Canale [ai], F. Cao [z], L. Carroll [aa], C. Caso [u], E. Castelli [p], M.V. Castillo Gimenez [g], A. Cattai [i], F.R. Cavallo [aj], L. Cerrito [ai], M. Chapkin [w], P. Charpentier [i], P. Checchia [ae], G.A. Chelkov [f], L. Chevalier [c], P. Chliapnikov [w], V. Chorowicz [n], R. Cirio [ab], M.P. Clara [ab], P. Collins [s], J.L. Contreras [ak], R. Contri [u], G. Cosme [o], F. Couchot [o], H.B. Crawley [a,l], D. Crennell [d], G. Crosetti [u], N. Crosland [s], M. Crozon [v], J. Cuevas Maestro [ah], S. Czellar [af], S. Dagoret [o], E. Dahl-Jensen [am], B. Dalmagne [o], M. Dam [i], G. Damgaard [am], G. Darbo [u], E. Daubie [z], P.D. Dauncey [s], M. Davenport [i], P. David [n], A. De Angelis [p], M. De Beer [c], H. De Boeck [z], W. De Boer [l], C. De Clercq [z], M.D.M. De Fez Laso [g], N. De Groot [ac], C. De La Vaissiere [n], B. De Lotto [p], A. De Min [r], C. Defoix [v], D. Delikaris [i], S. Delorme [i], P. Delpierre [v], N. Demaria [ab], J. Derkaoui [ab,*], L. Di Ciaccio [ai], H. Dijkstra [i], F. Djama [y], J. Dolbeau [v], M. Donszelmann [ac], K. Doroba [an], M. Dracos [i], J. Drees [t], M. Dris [ao], Y. Dufour [v], W. Dulinski [y], R. Dzhelyadin [w], L.-O. Eek [ad], P.A.-M. Eerola [af], T. Ekelof [ad], G. Ekspong [m], A. Elliot Peisert [ae], J.-P. Engel [y], D. Fassouliotis [ao], M. Fernandez Alonso [ah],

A. Ferrer [g], T.A. Filippas [ao], A. Firestone [a ℓ], H. Foeth [i], E. Fokitis [ao], P. Folegati [p], F. Fontanelli [u], H. Forsbach [t], B. Franek [d], P. Frenkiel [v], D.C. Fries [ℓ], A.G. Frodesen [h], R. Fruhwirth [b], F. Fulda-Quenzer [o], K. Furnival [aa], H. Furstenau [ℓ], J. Fuster [i], J.M. Gago [a], G. Galeazzi [ae], D. Gamba [ab], C. Garcia [g], J. Garcia [ah], U. Gasparini [ac], P. Gavillet [i], E.N. Gazis [ao], J.-P. Gerber [y], P. Giacomelli [aj], K.-W. Glitza [t], R. Gokieli [i], V.M. Golovatyuk [f], J.J. Gomez Y Cadenas [i], A. Goobar [m], G. Gopal [d], M. Gorski [an], V. Gracco [u], A. Grant [i], F. Grard [z], E. Graziani [q], M.-H. Gros [o], G. Grosdidier [o], B. Grossetete [n], S. Gumenyuk [w], J. Guy [d], F. Hahn [i], M. Hahn [ℓ], S. Haider [ac], Z. Hajduk [ac], A. Hakansson [e], A. Hallgren [ad], K. Hamacher [t], G. Hamel De Monchenault [c], F.J. Harris [s], B.W. Heck [i], I. Herbst [t], J.J. Hernandez [g], P. Herquet [z], H. Herr [i], I. Hietanen [af], E. Higon [g], H.J. Hilke [i], S.D. Hodgson [s], T. Hofmokl [an], R. Holmes [a ℓ], S.-O. Holmgren [m], D. Holthuizen [ac], P.F. Honore [v], J.E. Hooper [am], M. Houlden [aa], J. Hrubec [b], P.O. Hulth [m], K. Hultqvist [m], D. Husson [v], B.D. Hyams [i], P. Ioannou [j], D. Isenhower [i], P.-S. Iversen [h], J.N. Jackson [aa], P. Jalocha [ap], G. Jarlskog [e], P. Jarry [c], B. Jean-Marie [o], E.K. Johansson [m], D. Johnson [aa], M. Jonker [i], L. Jonsson [e], P. Juillot [y], G. Kalkanis [j], G. Kalmus [d], G. Kantardjian [i], F. Kapusta [n], S. Katsanevas [j], E.C. Katsoufis [ao], R. Keranen [af], J. Kesteman [z], B.A. Khomenko [f], N.N. Khovanski [f], B. King [aa], N.J. Kjaer [am], H. Klein [i], W. Klempt [i], A. Klovning [h], P. Kluit [ac], J.H. Koehne [ℓ], B. Koene [ac], P. Kokkinias [x], M. Kopf [ℓ], M. Koratzinos [i], K. Korcyl [ap], A.V. Korytov [f], B. Korzen [i], V. Kostukhin [w], C. Kourkoumelis [j], T. Kreuzberger [b], J. Krolikowski [an], U. Kruener-Marquis [t], W. Krupinski [ap], W. Kucewicz [r], K. Kulka [e], K. Kurvinen [af], C. Lacasta [g], C. Lambropoulos [x], J.W. Lamsa [a ℓ], L. Lanceri [p], V. Lapin [w], J.-P. Laugier [c], R. Lauhakangas [af], G. Leder [b], F. Ledroit [v], J. Lemonne [z], G. Lenzen [t], V. Lepeltier [o], A. Letessier-Selvon [n], D. Liko [b], E. Lieb [t], E. Lillethun [h], J. Lindgren [af], A. Lipniacka [an], I. Lippi [ae], R. Llosa [ak], B. Loerstad [e], M. Lokajicek [f], J.G. Loken [s], M.A. Lopez Aguera [ah], A. Lopez-Fernandez [o], M. Los [ac], D. Loukas [x], A. Lounis [y], J.J. Lozano [g], R. Lucock [d], P. Lutz [v], L. Lyons [s], G. Maehlum [i], J. Maillard [v], A. Maltezos [x], S. Maltezos [ao], F. Mandl [b], J. Marco [ah], M. Margoni [ae], J.-C. Marin [i], A. Markou [x], S. Marti [g], L. Mathis [v], F. Matorras [ah], C. Matteuzzi [r], G. Matthiae [ai], M. Mazzucato [ae], M. Mc Cubbin [aa], R. Mc Kay [a ℓ], R. Mc Nulty [aa], E. Menichetti [ab], G. Meola [u], C. Meroni [r], W.T. Meyer [a ℓ], M. Michelotto [ae], W.A. Mitaroff [b], G.V. Mitselmakher [f], U. Mjoernmark [e], T. Moa [m], R. Moeller [am], K. Moenig [t], M.R. Monge [u], P. Morettini [u], H. Mueller [ℓ], H. Muller [i], W.J. Murray [d], G. Muyatt [s], F. Naraghi [n], U. Nau-Korzen [t], F.L. Navarria [aj], P. Negri [r], B.S. Nielsen [am], B. Nijjhar [aa], V. Nikolaenko [w], V. Obraztsov [w], A.G. Olshevski [f], R. Orava [af], A. Ostankov [w], A. Ouraou [c], R. Pain [n], H. Palka [ac], T. Papadopoulou [ao], L. Pape [i], A. Passeri [q], M. Pegoraro [ae], V. Perevozchikov [w], M. Pernicka [b], A. Perrotta [aj], F. Pierre [c], M. Pimenta [a], O. Pingot [z], A. Pinsent [s], M.E. Pol [a], G. Polok [ap],

P. Poropat [p], P. Privitera [ℓ], A. Pullia [r], J. Pyyhtia [af], D. Radojicic [s], S. Ragazzi [r], W.H. Range [aa], P.N. Ratoff [s], A.L. Read [ag], N.G. Redaelli [r], M. Regler [b], D. Reid [aa], P.B. Renton [s], L.K. Resvanis [j], F. Richard [o], M. Richardson [aa], J. Ridky [f], G. Rinaudo [ab], I. Roditi [i], A. Romero [ab], I. Roncagliolo [u], P. Ronchese [ae], C. Ronnqvist [af], E.I. Rosenberg [a,ℓ], U. Rossi [aj], E. Rosso [i], P. Roudeau [o], T. Rovelli [aj], W. Ruckstuhl [ac], V. Ruhlmann [c], A. Ruiz [ah], K. Rybicki [ap], H. Saarikko [af], Y. Sacquin [c], J. Salt [g], E. Sanchez [g], J. Sanchez [ak], M. Sannino [u], M. Schaeffer [y], S. Schael [ℓ], H. Schneider [ℓ], F. Scuri [p], A.M. Segar [s], R. Sekulin [d], M. Sessa [p], G. Sette [u], R. Seufert [ℓ], R.C. Shellard [a], P. Siegrist [c], S. Simonetti [u], F. Simonetto [ae], A.N. Sissakian [f], T.B. Skaali [ag], G. Skjevling [ag], G. Smadja [k,c], G.R. Smith [d], N. Smirnov [w], R. Sosnowski [an], T.S. Spassoff [f], E. Spiriti [q], S. Squarcia [u], H. Staeck [t], C. Stanescu [q], G. Stavropoulos [x], F. Stichelbaut [z], A. Stocchi [o], J. Strauss [b], R. Strub [y], C.J. Stubenrauch [i], M. Szczekowski [an], M. Szeptycka [an], P. Szymanski [an], T. Tabarelli [r], S. Tavernier [z], O. Tchikilev [w], G.E. Theodosiou [x], A. Tilquin [aq], J. Timmermans [ac], V.G. Timofeev [f], L.G. Tkatchev [f], T. Todorov [f], D.Z. Toet [ac], L. Tortora [q], M.T. Trainor [s], D. Treille [i], U. Trevisan [u], W. Trischuk [i], G. Tristram [v], C. Troncon [r], A. Tsirou [i], E.N. Tsyganov [f], M. Turala [ap], R. Turchetta [y], M.-L. Turluer [c], T. Tuuva [af], I.A. Tyapkin [f], M. Tyndel [d], S. Tzamarias [i], B. Ueberschaer [t], S. Ueberschaer [t], O. Ullaland [i], V.A. Uvarov [w], G. Valenti [aj], E. Vallazza [ab], J.A. Valls Ferrer [g], G.W. Van Apeldoorn [ac], P. Van Dam [ac], W.K. Van Doninck [z], N. Van Eijndhoven [i], C. Vander Velde [z], J. Varela [a], P. Vaz [a], G. Vegni [r], J. Velasco [g], L. Ventura [ae], W. Venus [d], F. Verbeure [z], L.S. Vertogradov [f], L. Vibert [n], D. Vilanova [c], E.V. Vlasov [w], A.S. Vodopyanov [f], M. Vollmer [t], S. Volponi [aj], G. Voulgaris [j], M. Voutilainen [af], V. Vrba [q], H. Wahlen [t], C. Walck [m], F. Waldner [p], M. Wayne [a,ℓ], P. Weilhammer [i], J. Werner [t], A.M. Wetherell [i], J.H. Wickens [z], J. Wikne [ag], G.R. Wilkinson [s], W.S.C. Williams [s], M. Winter [y], D. Wormald [ag], G. Wormser [o], K. Woschnagg [ad], N. Yamdagni [m], P. Yepes [i], A. Zaitsev [w], A. Zalewska [ap], P. Zalewski [an], E. Zevgolatakos [x], G. Zhang [t], N.I. Zimin [f], M. Zito [c], R. Zitoun [n], R. Zukanovich Funchal [v], G. Zumerle [ae] and J. Zuniga [g]

[a] *LIP, Av. Elias Garcia 14-1e, P-1000 Lisbon Codex, Portugal*
[b] *Institut für Hochenergiephysik, Österreichische Akademie der Wissenschaften, Nikolsdorfergasse 18, A-1050 Vienna, Austria*
[c] *DPhPE, CEN-Saclay, F-91191 Gif-Sur-Yvette Cedex, France*
[d] *Rutherford Appleton Laboratory, Chilton, Didcot OX11 0QX, UK*
[e] *Department of Physics, University of Lund, Sölvegatan 14, S-22363 Lund, Sweden*
[f] *Joint Institute for Nuclear Research, Dubna, Head Post Office, P.O. Box 79, SU-101 000 Moscow, USSR*
[g] *Instituto de Fisica Corpuscular (IFIC), Centro Mixto Universidad de Valencia-SCIC, Avda. Dr. Moliner 50, E-46100 Burjassot (Valencia), Spain*
[h] *Department of Physics, University of Bergen, Allégaten 55, N-5007 Bergen, Norway*
[i] *CERN, CH-1211 Geneva 23, Switzerland*
[j] *Physics Laboratory, University of Athens, Solonos Street 104, GR-10680 Athens, Greece*
[k] *Université Claude Bernard de Lyon, 43 Bd du 11 Novembre 1918, F-69622 Villeurbanne Cedex, France*

* Permanent address: Département de Physique, Faculté des Sciences d'Oujda, Maroc.

[l] Institut für Experimentelle Kernphysik, Universität Karlsruhe, Postfach 6980, W-7500 Karlsruhe 1, Germany
[m] Institute of Physics, University of Stockholm, Vanadisvägen 9, S-113 46 Stockholm, Sweden
[n] LPNHE, Universités Paris VI et VII, Tour 33 (RdC), 4 place Jussieu, F-75230 Paris Cedex 05, France
[o] Laboratoire de l'Accélérateur Linéaire, Université de Paris-Sud, Bâtiment 200, F-91405 Orsay, France
[p] Dipartimento di Fisica, Università di Trieste and INFN, Via A. Valerio 2, I-34127 Trieste, Italy and Istituto di Fisica, Università di Udine, Via Larga 36, I-33100 Udine, Italy
[q] Istituto Superiore di Sanità, Istituto Nazionale di Fisica Nucleare (INFN), Viale Regina Elena 299, I-00161 Rome, Italy
[r] Dipartimento di Fisica, Università di Milano and INFN, Via Celoria 16, I-20133 Milan, Italy
[s] Nuclear Physics Laboratory, University of Oxford, Keble Road, Oxford OX1 3RH, UK
[t] Fachbereich Physik, University of Wuppertal, Pf. 100 127, W-5600 Wuppertal 1, Germany
[u] Dipartimento di Fisica, Università di Genova and INFN, Via Dodecaneso 33, I-16146 Genoa, Italy
[v] Laboratoire de Physique Corpusculaire, Collège de France, 11 place M. Berthelot, F-75231 Paris Cedex 5, France
[w] Institute for High Energy Physics, Serpukhov, P.O. Box 35, SU-142 284 Protvino (Moscow Region), USSR
[x] Institute of Nuclear Physics, N.C.S.R. Demokritos, P.O. Box 60228, GR-15310 Athens, Greece
[y] Division des Hautes Energies, CRN-Groupe DELPHI and LEPSI, B.P. 20 CRO, F-67037 Strasbourg Cedex, France
[z] Physics Department, Universitaire Instelling Antwerpen, Universiteitsplein 1, B-2610 Wilrijk, Belgium and IIHE, ULB-VUB, Pleinlaan 2, B-1050 Brussels, Belgium and Service de Physique des Particules Elémentaires, Faculté des Sciences, Université de l'Etat Mons, Av. Maistriau 19, B-7000 Mons, Belgium
[aa] Department of Physics, University of Liverpool, P.O. Box 147, Liverpool L69 3BX, UK
[ab] Dipartimento di Fisica Sperimentale, Università di Torino and INFN, Via P. Giuria 1, I-10125 Turin, Italy
[ac] NIKHEF-H, Postbus 41882, NL-1009 DB Amsterdam, The Netherlands
[ad] Department of Radiation Sciences, University of Uppsala, P.O. Box 535, S-751 21 Uppsala, Sweden
[ae] Dipartimento di Fisica, Università di Padova and INFN, Via Marzolo 8, I-35131 Padua, Italy
[af] Research Institute for High Energy Physics, University of Helsinki, Siltavuorenpenger 20 C, SF-00170 Helsinki 17, Finland
[ag] Physics Department, University of Oslo, Blindern, N-1000 Oslo 3, Norway
[ah] Facultad de Ciencias, Universidad de Santander, av. de los Castros, E-39005 Santander, Spain
[ai] Dipartimento di Fisica, Università di Roma II and INFN, Tor Vergata, I-00173 Rome, Italy
[aj] Dipartimento di Fisica, Università di Bologna and INFN, Via Irnerio 46, I-40126 Bologna, Italy
[ak] Departamento de Fisica Atomica Molecular y Nuclear, Universidad Complutense, Avda. Complutense s/n, E-28040 Madrid, Spain
[al] Ames Laboratory and Department of Physics, Iowa State University, Ames IA 50011, USA
[am] Niels Bohr Institute, Blegdamsvej 17, DK-2100 Copenhagen Ø, Denmark
[an] Institute for Nuclear Studies, and University of Warsaw, Ul. Hoża 69, PL-00681 Warsaw, Poland
[ao] Physics Department, National Technical University, Zografou Campus, GR-15773 Athens, Greece
[ap] High Energy Physics Laboratory, Institute of Nuclear Physics, Ul. Kawiory 26 a, PL-30055 Cracow 30, Poland
[aq] Faculté des Sciences de Luminy, Université d'Aix-Marseille II Case 907-70, route Léon Lachamp, F-13288 Marseille Cedex 09, France

Received 5 August 1991
Accepted for publication 26 August 1991

From measurements of the cross sections for $e^+e^- \to$ hadrons and the cross sections and forward–backward charge-asymmetries for $e^+e^- \to e^+e^-$, $\mu^+\mu^-$ and $\tau^+\tau^-$ at several centre-of-mass energies around the Z^0 pole with the DELPHI apparatus, using approximately 150000

hadronic and leptonic events from 1989 and 1990, one determines the following Z^0 parameters: the mass and total width $M_Z = 91.177 \pm 0.022$ GeV, $\Gamma_Z = 2.465 \pm 0.020$ GeV, the hadronic and leptonic partial widths $\Gamma_h = 1.726 \pm 0.019$ GeV, $\Gamma_\ell = 83.4 \pm 0.8$ MeV, the invisible width $\Gamma_{inv} = 488 \pm 17$ MeV, the ratio of hadronic over leptonic partial widths $R_Z = 20.70 \pm 0.29$ and the Born level hadronic peak cross section $\sigma_0 = 41.84 \pm 0.45$ nb. A flavour-independent measurement of the leptonic cross section gives very consistent results to those presented above ($\Gamma_\ell = 83.7 \pm 0.8$ MeV). From these results the number of light neutrino species is determined to be $N_\nu = 2.94 \pm 0.10$. The individual leptonic widths obtained are: $\Gamma_e = 82.4 \pm 1.2$ MeV, $\Gamma_\mu = 86.9 \pm 2.1$ MeV and $\Gamma_\tau = 82.7 \pm 2.4$ MeV. Assuming universality, the squared vector and axial-vector couplings of the Z^0 to charged leptons are: $\bar{V}_\ell^2 = 0.0003 \pm 0.0010$ and $\bar{A}_\ell^2 = 0.2508 \pm 0.0027$. These values correspond to the electroweak parameters: $\rho_{eff} = 1.003 \pm 0.011$ and $\sin^2\theta_W^{eff} = 0.241 \pm 0.009$. Within the Minimal Standard Model (MSM), the results can be expressed in terms of a single parameter: $\sin^2\theta_W^{\overline{MS}} = 0.2338 \pm 0.0027$. All these values are in good agreement with the predictions of the MSM. Fits yield $43 < m_{top} < 215$ GeV at the 95% level. Finally, the measured values of Γ_Z and Γ_{inv} are used to derive lower mass bounds for possible new particles.

1. Introduction

LEP experiments have the unique ability to measure the Z^0 resonance parameters with great precision. This allows not only a determination of the Z^0 mass, one of the cornerstones of the Minimal Standard Model (MSM), but also severe consistency checks of the MSM predictions and the possibility to detect new features beyond it. As the size of any departure from the MSM is expected to be rather small, the Z^0 resonance parameters have to be determined with very high precision. This calls for the maximum possible LEP luminosity and for a thorough study of the systematic uncertainties affecting the parameter measurements.

The total and the invisible widths are very sensitive to the production of new particles predicted by extensions of or alternatives to the MSM. In the absence of direct observation of a new particle, their measured values can be used to derive lower mass bounds for these particles. In addition, the invisible width leads directly to a measurement of the number of light neutrino species.

The parameters of the hadronic and leptonic lineshape of the Z^0 were measured by the DELPHI collaboration in 1989 [1,2] on the basis of a total integrated luminosity of 0.57 pb^{-1}. The measurement showed that the number of light neutrino species is consistent with three, the alternative hypotheses of two or four light Dirac neutrino generations being clearly ruled out. However, the number of neutrino generations should be measured as accurately as possible. Indeed a fourth massive Dirac neutrino would give an effective number of light neutrinos slightly larger than three whereas this number would be slightly below three if the fourth-generation neutrino were right-handed [3]. The existence of relatively light particles from models beyond the MSM (e.g. supersymmetric extensions to the MSM) would also lead to deviations from an apparent integral value for the number of light neutrinos.

Within the framework of the MSM, there are significant electroweak radiative corrections to the Born level formulae for high energy e^+e^- annihilation cross sections. These corrections depend on the mass of the Z^0, M_Z and the unknown masses of the top quark, m_{top}, and the Higgs boson, M_H. The sensitivity of the present data to M_H is very small but a comparison of the predictions of the MSM with the measurements of these cross sections (and the charge asymmetries of leptons) leads to bounds on the allowed range of m_{top}. Alternatively, it is possible to absorb some of the electroweak corrections in terms of effective couplings of the Z^0 to fermions, or in terms of an effective weak mixing angle. This latter approach facilitates the comparison of the results from different types of experiments.

This paper reports on the determination of the Z^0 resonance parameters and the strength of the Z^0 couplings to charged leptons, from measurements of the cross sections for $e^+e^- \rightarrow$ hadrons and the cross sections and forward–backward charge-asymmetries for $e^+e^- \rightarrow$ charged leptons at several centre-of-mass energies close to the Z^0 peak. It is based on a total of 150 000 hadronic and leptonic decays of the Z^0 recorded in the DELPHI detector between August 1989 and August 1990. Subsamples of 125 000 hadronic events and 10 000 leptonic events, collected under good data taking conditions have been selected, corresponding to a total integrated luminosity of 5.88 pb^{-1} for hadrons and 4.35–4.97 pb^{-1} for leptons (the value varying for the different leptonic analyses).

Compared to the 1989 measurements, those from 1990 benefit from more than ten times larger statistics, improved running conditions, reduced systematic uncertainties (in particular those affecting the luminosity determination) and a better knowledge of the beam energy. Furthermore, the published 1989 hadronic data were re-analysed, taking into account the improvements from the analysis of the 1990 data.

The paper is organised as follows. After a brief review of the apparatus involved in these analyses (sect. 2), the luminosity measurement is described in detail (sect. 3). A short description of the trigger for hadronic and leptonic events is given in sect. 4. The selection of hadronic decays of the Z^0 is described in sect. 5 together with the computation of the cross sections. The selection of leptonic decays of the Z^0 is described in sect. 6 along with the determination of the cross sections and forward–backward charge-asymmetries. In sect. 7 the fit results are presented, followed by the interpretation of these results in sect. 8. Finally, the results are summarized in sect. 9.

2. Apparatus

A detailed description of the DELPHI apparatus can be found in ref. [4]. For the present analysis the following parts of the detector were relevant:

(i) For the measurement of charged particles the Microvertex Detector (VD) *, the Inner Detector (ID), the Time Projection Chamber (TPC), the Outer Detector (OD) and the Forward Chambers A an B (FCA, FCB)

(ii) For the measurement of the electromagnetic energy of High-density Projection Chamber (HPC) and the Forward ElectroMagnetic Calorimeter (FEMC); these detectors were also used for identifying minimum ionizing particles;

(iii) for the measurement of the hadronic energy and muon identification the Hadron Calorimeter (HCAL), which covered both the barrel and endcap regions;

(iv) for muon identification the barrel (MUB) and endcap (MUF) muon chambers;

(v) for the trigger (sect. 4), besides the detectors mentioned above, the barrel Time-Of-Flight counters (TOF), the endcap scintillators (HOF) and a scintillator layer embedded in HPC;

(vi) for the measurement of the luminosity (sect. 3) the Small Angle Tagger (SAT).

The ID and TPC cover the angular range $20° < \theta < 160°$ (in the DELPHI coordinate system θ is the polar angle defined with respect to the beam axis and ϕ is the azimuthal angle about this axis), the OD covers the range $43° < \theta < 137°$ and FCA/FCB cover the range $11° < \theta < 33°$ and $147° < \theta < 169°$. Within the barrel region (defined as the angular acceptance of the OD) the momentum resolution obtained for 46 GeV muons is $\sigma_p/p = 0.08$, whereas in the part of the endcap region covered by FCA/FCB and the ID/TPC, $\sigma_p/p = 0.12$. The MUB covers the interval $52° < \theta < 128°$ whilst the MUF extends over the range $9° < \theta < 43°$ and $137° < \theta < 171°$.

The HPC has the same angular coverage as the OD, whilst the FEMC covers an interval slightly larger than the FCA/FCB. The HCAL covers the entire barrel and endcap regions over the range $10° < \theta < 170°$. The energy resolutions (σ_E/E) of the electromagnetic calorimeters for 46 GeV electrons are 0.08 (HPC) and 0.05 (FEMC). The HCAL energy resolution is $1.0/\sqrt{E(\mathrm{GeV})}$

As an illustration, a hadronic event in the barrel part of the DELPHI detector is shown in fig. 1.

3. Luminosity measurement

The luminosity measurement was based on the observation of small-angle Bhabha scattering in the SAT calorimeters (constructed with lead sheets and plastic scintillating fibres), each one containing 288 "towers" or readout elements (see fig. 2).

* The VD, which was operated during most of the 1990 data collection period, was used in the alignment procedure of the barrel tracking detectors, but was not used directly in the analysis described here.

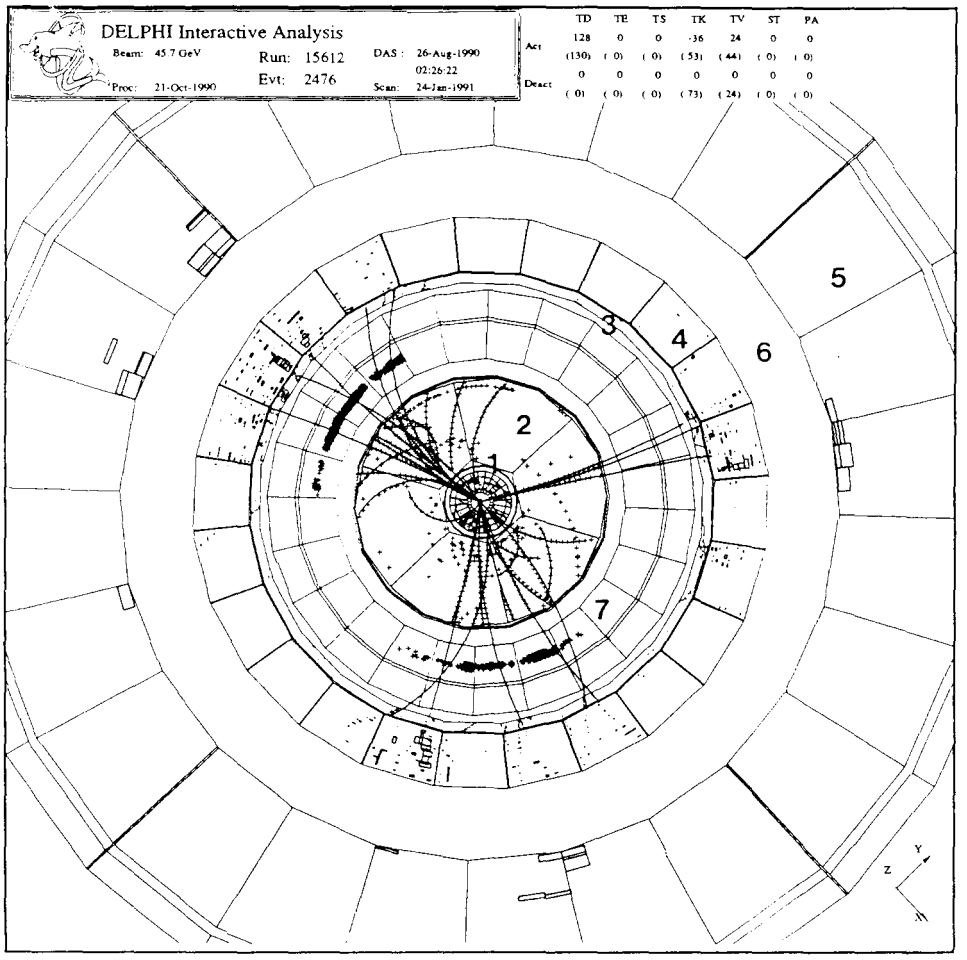

Fig. 1. Hadronic event in the barrel detectors of the DELPHI apparatus. The barrel detectors used for the analysis are the ID(1), the TPC(2), the OD(3), the HPC(4) and the HCAL(5). The solenoid is indicated by (6). The Barrel RICH(7), for which one sees the hits due to photoelectrons, was not used in the present analysis.

The triggers for luminosity events were based on pulse-height sums of 24 channels in 24 overlapping sectors of 30° per endcap. The primary trigger required coplanar coincidence of energy depositions larger than 10 GeV in each calorimeter. In order to measure the primary trigger efficiency, a single arm trigger requiring energy larger than 30 GeV was operated. This trigger was downscaled in order to keep the rate at a tolerable level. Based on about 1500 observed events, the primary trigger was measured to be 100% efficient. The statistical accuracy of the measurement was 0.13%.

To define accurately the fiducial volume a precisely machined lead mask was installed in front of the entrance of one of the calorimeters. The mask covered the

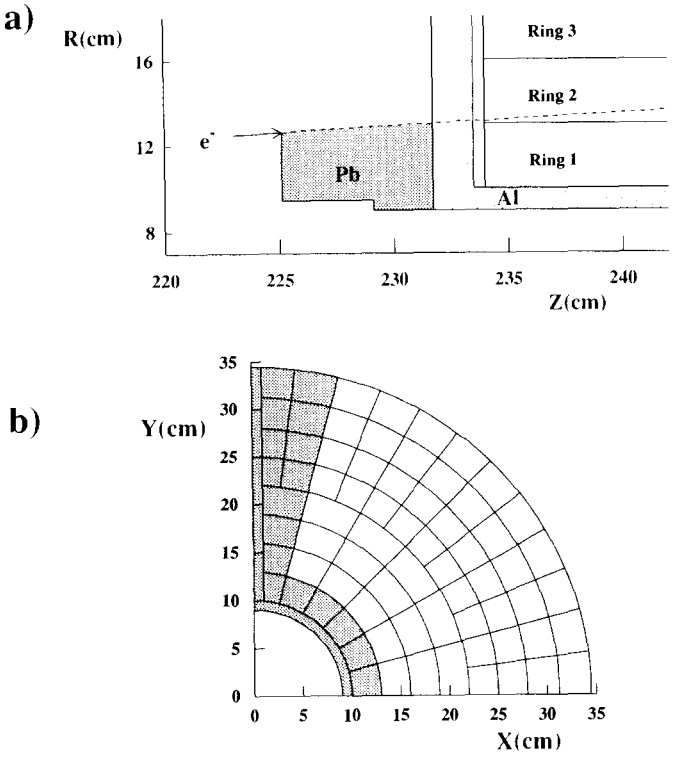

Fig. 2. The Small Angle Tagger calorimeter. (a) Side view showing the lead mask in front of calorimeter. (b) Segmentation in one quadrant. The shaded area indicates the coverage of the mask.

inner 3 cm of the calorimeter acceptance. The cone-shaped outer surface pointed back to the nominal interaction point. For the last three-quarters of the data recorded in 1990 an additional "ϕ-mask", which covered $\pm 15^\circ$ around the vertical junction between the two calorimeter half barrels, was installed. The radius of the ring and the width of the ϕ-mask were each known to better than 0.1 mm. With a thickness of 12 radiation lengths the mask reduced the energy deposited in the calorimeters by an average of 85%. There was thus a clear separation between electrons passing through the mask and electrons hitting the SAT outside the mask. Detailed shower simulations showed that the transition region at the edge of the mask was about 0.4 mm wide.

To minimize the sensitivity to displacements of the interaction point it is common to use a method of asymmetric restricted acceptances in the two calorimeters [5]. This is, however, not possible with the lead mask technique, which results in a restricted acceptance in one arm only and a corresponding sensitivity of 0.83% per cm of longitudinal displacement. The linear dependence on lateral displacements still cancels, and only a very small second-order dependence remains. The average position of the interaction point along the beam axis was

measured for each LEP run by the TPC with an absolute precision of 1 mm. The position of the lead mask relative to the TPC was measured with a similar precision. This leads to a 0.13% contribution to the systematic uncertainty on the luminosity.

The calculation of the visible SAT cross section (i.e. the expected $e^+e^- \to e^+e^-$ cross section within the angular acceptance of the SAT) was based on a detailed detector simulation of Bhabha events generated by the event generator BABAMC [6]. The event generator, which includes $O(\alpha)$ corrections, where α is the electromagnetic coupling constant, was checked against semi-analytical calculations [7]. The simulation was performed at the peak of the Z^0 resonance. The simulated events were analysed by the same analysis programs as the real data. The visible cross section was found to be $\sigma_B = (27.12 \pm 0.04)$ nb, where the error is statistical only. The detector simulation was improved compared to earlier work [1] by the introduction of light attenuation in the fibres and by a description of the calorimeter as separate lead and scintillator layers. The extrapolation of the cross section to other energies was performed using the predicted $1/s$ dependence from QED, together with a small deviation due to electroweak processes (mainly interference), which was calculated by the event generator.

The analysis was based on the reconstructed energy and position of showers. Only information from the shower with the highest readout element multiplicity in each calorimeter was used. The following selection criteria were applied:

(i) The cluster centroid in the masked calorimeter was required not to be in the outer ring of readout elements to avoid edge effects at the calorimeter surface. Biases in the radius reconstruction in this region can be of the order of 2 mm, resulting in a 0.25% contribution to the overall uncertainty.

(ii) The cluster centroid in the non-masked calorimeter was required to be at least 2.5 cm away from the inner radius to reduce background. The cut is at a smaller radius than the one provided by the mask in the opposite calorimeter. It applies therefore only to non-collinear events, and removed only 2.5% of the data. The contribution to the uncertainty was estimated to be 0.25%.

(iii) To avoid contamination from events passing inside the mask and entering the calorimeter through the inner surface, it was required that all clusters have less than half of their energy deposited in the inner ring of the masked calorimeter. Based on the observed separation of the signal from the background, this cut was estimated to contribute 0.1% to the overall uncertainty.

(iv) Events with a cluster centroid closer than 4 cm to the inner radius were rejected if the cluster energy was greater than $1.5 \times E_{\mathrm{BEAM}}$, where E_{BEAM} is the beam energy. Low-energy photons and minimum ionizing particles which hit the readout system (fibres, light guides, and photodiodes) can simulate high-energy depositions. This was a particular problem at small radii where the rate of partially contained showers was large. This cut removed 0.16% of the sample and the uncertainty of the procedure was estimated to be of the same size.

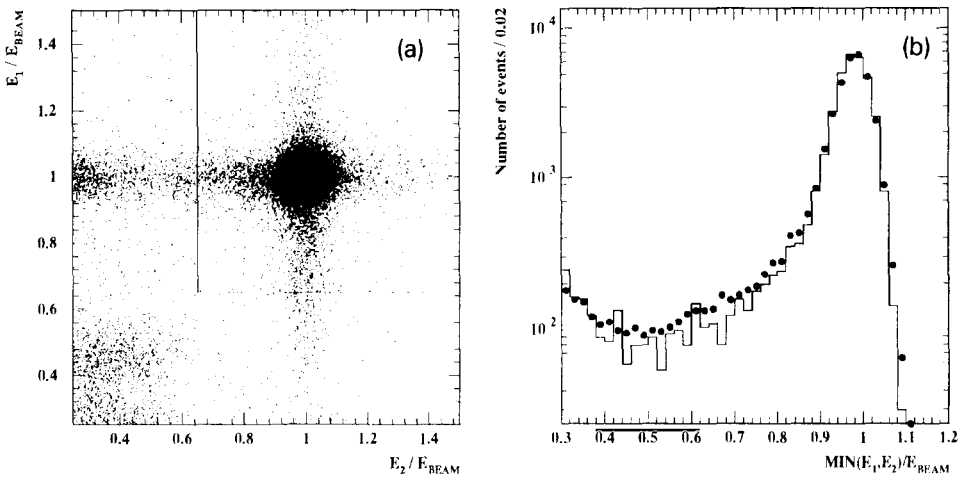

Fig. 3. Energy distributions for luminosity events. (a) Two-dimensional plot showing the energy in the two calorimeters after all cuts except the energy cut have been applied. E_2 refers to the masked calorimeter. The accumulation of events around $E_2 = 0.3 \times E_{BEAM}$ and $E_1 = E_{BEAM}$ is due to electrons which traverse the lead mask. (b) Energy spectrum of the least energetic cluster. The points are from real data, the solid line is from Monte Carlo simulations.

(v) Events with a cluster centroid in the masked calorimeter closer than 8° to the vertical junction were rejected. Due to the ϕ-mask, large energy depositions should in principle not occur in this region. However, the junction constituted a window of light material through which leakage of low energy particles onto the readout system was possible. The 0.15% of the data removed by the cut was compatible with this effect. An uncertainty contribution of the same size was estimated.

(vi) To suppress background from off-momentum electrons, the acoplanarity angle between the two clusters was required to be less than 20°.

(vii) The energy is both calorimeters was required to be greater than $0.65 \times E_{BEAM}$. Due to the lead mask this is also an implicit fiducial volume cut. Fig. 3 shows the energy deposited in calorimeter 1 (unmasked) and 2 (masked), and the distribution of the smaller of the two energies for Monte Carlo and real data. From the size of the discrepancy between the two distributions, a 0.4% contribution to the overall uncertainty was estimated.

(viii) For the first quarter of the data recorded in 1990, during which the ϕ-mask was not installed, the cluster centroid in the masked calorimeter was required to be one 15° azimuthal sector away from the vertical dead region. A 0.4% uncertainty contribution was assigned to this cut. This is less than the 1% assigned previously [1] due to a precise survey of the SAT internal geometry.

Possible backgrounds to small-angle Bhabha scattering include both e^+e^- interactions and accidentally coincident off-momentum particles from beam–gas interactions. The backgrounds from the process $e^+e^- \to \gamma\gamma$ as well as from

TABLE 1
Contributions to the systematic uncertainty on the luminosity measurement

Contribution	Uncertainty (%)
Mask radius	0.15
ϕ acceptance	0.10
Outer radius masked calorimeter	0.25
Inner radius unmasked calorimeter	0.25
Interaction point position	0.13
Energy cut	0.40
Fake high-energy deposits at small radii	0.16
Data behind ϕ-mask	0.15
Less than half of energy in inner ring	0.10
Monte Carlo statistics	0.15
Trigger efficiency	0.13
Off-momentum background	0.14
Dead channel correction	0.16
Miscellaneous	0.30
Total *experimental* uncertainty	0.8

two-photon interactions, $e^+e^- \to e^+e^-X$, were calculated to be negligible. An analysis of the sidebands of the acoplanarity distributions for different energy regions showed that the background from off-momentum electrons was less than 0.14%. An uncertainty of the same size was assigned.

The integrated luminosity L for each data-taking period was determined from the relation

$$L = \frac{N_{ev} - N_{bk}}{\sigma_B} \tag{1}$$

where N_{ev} and N_{bk} are the number of selected Bhabha events and the number of background events respectively.

The contributions to the experimental uncertainty are summarized in table 1. The total uncertainty due to geometrical effects, including the interaction point position, is 0.4%. A 1.6% correction to the luminosity for dead channels was estimated from the data. The uncertainty of 0.16% is due to the difficulty of calibrating the energy response near the edge of dead readout elements.

The miscellaneous item in the table is present to take into account differences between the simulated and real distributions other than the energy distribution. Some of the differences can be attributed to the effects of fake high-energy depositions and the non-ideal geometry of the calorimeter segmentation. The estimate of 0.3% covers systematic uncertainties which may be present but remain obscured by these effects.

The overall experimental uncertainty is 0.8%. This is considerably smaller than the previously reported value of 2.1% [1]. To summarize, the improvement is due

to a better measurement of the trigger efficiency, the installation of the ϕ-mask, better understanding and treatment of the effects due to the fake high-energy depositions, precise surveys of the SAT internal and external geometry, improvements to the detector simulation, and increased Monte Carlo statistics.

The effect of higher-order initial state photon radiation on the small-angle Bhabha scattering cross section was studied in the leading-logarithm approximation by means of the new Monte Carlo event generator LUMLOG [8]. The correction to the first-order result was found to be small ($< 0.2\%$) for the geometry of the SAT. This is in agreement with calculations based on a semianalytical approach [9]. Remaining contributions to the theoretical uncertainty stem from non-leading logarithmic corrections, vacuum polarization effects, and production of light fermion pairs from radiated photons. These contributions are estimated to add up to a total theoretical uncertainty of 0.5%. The total systematic uncertainty on the luminosity measurement is thus 0.9%.

Two thirds of the data recorded in 1989 (i.e. that data collected with the same annular mask as used in 1990) have been re-analysed in the way outlined above. The luminosity was found to differ by $+1.6\%$ compared to the 1989 analysis. The difference is less than the previously quoted experimental uncertainty of 2.1%. The main part of the difference (1.3%) originates from the precise measurement of the SAT internal geometry which revealed imperfections in the positions of the ϕ-borders between readout elements. The new total experimental systematic uncertainty for the 1989 data is 1.1%, with contributions similar to those for the data recorded in 1990. The luminosity corresponding to the first third of the 1989 data, which was recorded with a mask covering only the inner 2 cm of the calorimeter compared to the later 3 cm, has likewise been corrected by $+1.6\%$. The uncertainty on this data is now 2.0% compared to the 2.5% reported previously. As a consequence of the revised measurement of the luminosity, the 1989 hadronic cross sections [1] have been corrected by -1.6%.

4. The hadronic and leptonic event trigger

The DELPHI trigger system is described in detail in ref. [4]. The 1st-level (2nd-level) trigger decision is made 3 μs (42 μs) after the beam crossings. Consequently the apparatus is "dead" during the first beam crossing after a positive 1st-level decision, leading to a deadtime of about 1% for a typical 1st-level trigger rate of 400 Hz. However, no correction for this deadtime is required since the hadronic, leptonic and small-angle Bhabha (SAT) events were recorded with the same trigger and data acquisition system in order to ensure equal life-times. The 2nd-level trigger rate was typically a few Hz.

The following components of the detector are relevant for the triggering of hadronic and leptonic events. In the barrel region the trigger is based on several partially redundant components (a)–(d). It remained essentially unchanged during

1989 and 1990, apart from the addition of component (b) midway through 1990, whereas the triggers in the forward region (e)–(g) were improved in efficiency and stability in 1990 by including the tracking detectors, scintillators and endcap muon chambers. All components participate in the 1st-level trigger decision unless otherwise stated.

(a) A "double-arm track trigger" was made by coincidences of the ID and OD tracking chambers. Each detector provided signals for charged particles if there were hits in 3 out of 5 detector layers. This track trigger required signals in at least two OD quadrants, in coincidence with any signal from the ID.

(b) A "single-arm track trigger" was made by coincidences of the ID and OD tracking chambers at 1st level and the TPC at 2nd level. This track trigger required the coincidence of any signal in the ID or OD with a single "track", pointing to the beam interaction region, in the TPC.

(c) A 'scintillator trigger" was made by coincidences of the HPC and TOF scintillation counters. The HPC counters were sensitive to electromagnetic showers with an energy larger than 2 GeV while the TOF counters were sensitive to minimum ionising particles penetrating the electromagnetic calorimeter and the coil and to shower leakage from the calorimeter. The "scintillator trigger" was the OR of the following subtriggers:

- at least 2 TOF octants,
- at least 2 HPC octants,
- Coincidence of any TOF with any HPC octant.

(d) A fourth trigger component comprising TOF and OD signals was added to increase the redundancy in the barrel region. The trigger was formed by a coincidence of any TOF octant with any OD quadrant.

(e) A "forward electromagnetic" trigger consisted of a single-arm component (FEMC energy > 4.5 GeV) and a back-to-back component (FEMC energy in both endcaps > 3.0 GeV).

(f) A "forward majority" trigger required a coincidence of at least two of the following conditions, where the signals in each endcap were treated as independent.

- A coincidence of HOF signals from back-to-back quadrants.
- At least one track detected by coincidences between the forward tracking chambers FCA and FCB.
- An energy deposition of at least 3.0 GeV in a FEMC endcap.
- A coincidence of one OD quadrant with any ID signal.

(g) A "forward muon back-to-back" trigger was formed by a coincidence of the HOF at 1st level with the MUF at 2nd level. A signal from either HOF endcap was required to coincide with signals in back-to-back quadrants of the MUF endcaps.

The efficiency of the relevant subtriggers for the hadronic and leptonic events was measured using data samples which were recorded with independent subtriggers.

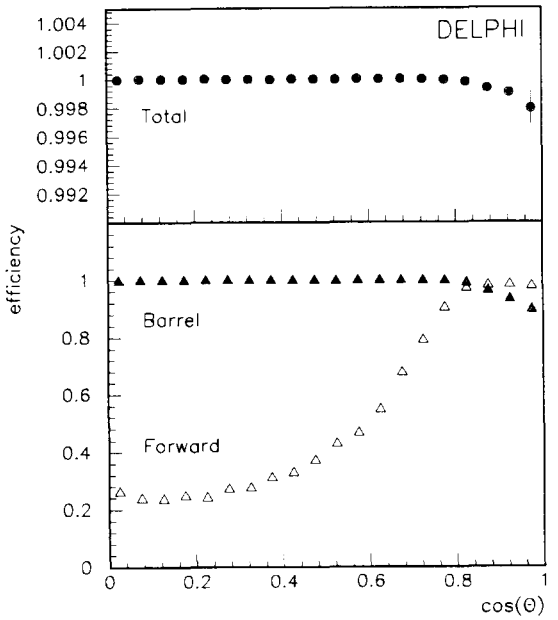

Fig. 4. Trigger efficiency for hadronic events as function of the polar angle of the sphericity axis of the event.

For the hadronic analysis, the barrel trigger was (a), (c) and (d) and, for the forward trigger, component (f). Fig. 4 summarizes the trigger efficiency for hadronic events, as a function of the polar angle of the sphericity axis of the event, for the forward and barrel triggers (shown separately) and, on a magnified scale, the overall efficiency of the trigger system. For values of $|\cos\theta_{\mathrm{sph}}|$ less than 0.65, i.e. the barrel region, the trigger efficiency was higher than 99.99%. Even in the very forward region it remained larger than 99.7%. For hadronic events recorded with trigger components missing, the corresponding correction to the overall efficiency was measured with data taken during periods in which all trigger components were fully operating. The loss of a component was simulated via the trigger pattern for each event. A correction between 0.2% and 2.5% was necessary for about 3% of the events. The uncertainty introduced by these corrections is negligible.

For the leptonic events, all the trigger components (a)–(g) were used, although for a given leptonic channel some were irrelevant e.g. (g) for electrons and (e) for muons. The trigger efficiencies for the leptonic events were found to be independent of polar angle within the barrel region. They were $(99.6 \pm 0.2)\%$ for e^+e^-, $(98.1 \pm 0.3)\%$ for $\mu^+\mu^-$, $(99.5 \pm 0.2)\%$ for $\tau^+\tau^-$ and $(99.0 \pm 0.3)\%$ for leptons selected without distinguishing their flavour. The slightly lower efficiency for $\mu^+\mu^-$ is due to a period of data taking when parts of the tracking detector trigger electronics were not correctly functioning. In the endcap region the average trigger efficiency for e^+e^- was $(99.9 \pm 0.1)\%$ whilst for $\mu^+\mu^-$ it varied slightly with $\cos\theta$,

giving an average efficiency over the combined barrel and endcap regions of $(96.5 \pm 0.3)\%$.

5. Hadronic event selection and cross sections

Hadronic events were selected with two complementary analyses, both of which required the same minimal multiplicity of charged particles. The first analysis (I) relied mainly on the energy of charged particles, whereas the second (II) relied instead on the energy deposited in the calorimeters.

Charged particles were retained if they satisfied the following selection criteria:

(i) momentum p in the range $0.4 < p < 50$ GeV;

(ii) relative error on momentum measurement less than 100%;

(iii) δr less than 4.0 cm, where δr is the distance of closest approach to the nominal interaction point in the radial direction;

(iv) $|\delta z|$ less than 10.0 cm, where δz is the distance of closest approach to the nominal interaction point along the beam direction;

(v) track length greater than 30.0 cm.

The cut values were chosen such as to allow a reliable measurement of the multiplicity and momentum of the selected charged particles.

5.1. ANALYSIS I

Hadronic events were accepted if:

(a) the total charged multiplicity is greater than or equal to 5;

(b) the energy sum E_1 is greater than 12% of the centre of mass energy, where $E_1 = E_{ch} + E^0_{FEMC}$. Assuming all charged particles to be pions, the total charged energy, E_{ch}, was taken as the sum of the energy of all selected charged particles. In order to increase the selection efficiency as well as to keep it rather insensitive to instabilities of the forward trigger and track reconstruction efficiencies, the energy of neutral particles, E^0_{FEMC}, deposited in the forward electromagnetic calorimeter (FEMC) was taken into account. Clusters were retained in the FEMC if they were not associated to a selected charged particle, if their reconstructed energy was between 0.4 and 50 GeV and if their polar angle was in the range $12°-35°$ or $145°-168°$.

The value of the energy cut was chosen such as to be least sensitive to the experimental uncertainty on the charged particle momenta. Fig. 5a shows the charged multiplicity distribution of the data before applying the cut of E_1. The distribution of the values of E_1 is displayed in fig. 5b for events with at least 5 charged particles.

A detailed Monte Carlo simulation of the detector, which included secondary interactions, the collection of electronic signals and their digitisation, was per-

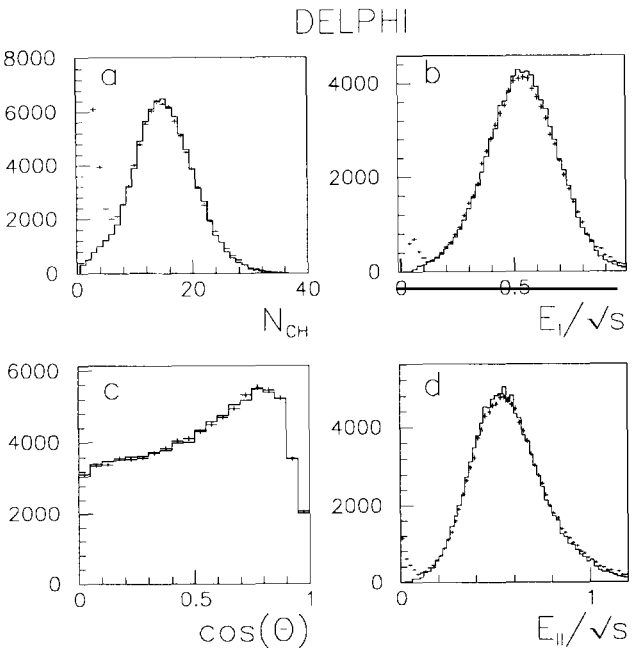

Fig. 5. Distributions of real events (points with statistical errors) and simulated events (continuous line) normalised to the selected data sample: (a) multiplicity of charged particles before the selection based on E_l or E_{ll}; (b) $E_l = E_{ch} + E^0_{FEMC}$ for events with at least 5 charged particles; (c) polar distribution of the sphericity axis; (d) calorimeter energy E_{ll} for events with at least 5 charged particles.

formed. The event generation relied on the DYMU3 event generator [10] and on the Lund 7.2 parton shower fragmentation model [11]. The same analysis was applied to the simulated and to the real events and good agreement between the two samples was observed. The final simulated charged multiplicity and total energy distributions are shown as continuous lines in fig. 5a and 5b. The contaminations from two-photon collisions and $\tau^+\tau^-$ events account for the difference between simulated and real multiplicity distributions for multiplicities between 5 and 8.

The selection efficiency for hadronic events was derived from the Monte Carlo simulation corrected for changes in the detector, trigger and track reconstruction inefficiencies at small polar angles and for the detection and reconstruction inefficiencies located around the edges of the TPC sectors. Overall these corrections reduced the efficiency by 0.8%. Fig. 5c shows the distribution of the polar angle of the sphericity axis for the data and for the corrected Monte Carlo events.

A total efficiency of $(96.3 \pm 0.4)\%$ was obtained. The various contributions to the uncertainty are summarized in table 2. The dominant source of systematic uncertainty comes from the 0.8% correction for inefficiencies applied to the simulated data sample. The corresponding uncertainty on the selection efficiency

TABLE 2
Contributions to the uncertainty on the hadronic event selection efficiency. The subtraction of the two-photon collision background introduces an additional uncertainty of 10 pb

Error source	Error (%)
Monte Carlo statistics	0.1
Correction for inefficiencies	0.3
Energy resolution	0.1
$\tau^+\tau^-$ contamination	0.1
Total	0.4

was estimated to be 0.3% at each collision energy and 0.05% from energy to energy.

5.2. ANALYSIS II

The second analysis is based on the total energy deposited in the calorimeters (i.e. HPC, FEMC, HCAL). Events were selected if:

(a) the total charged multiplicity is greater than or equal to 5;

(b) the total calorimetric energy E_{II} is greater than 16% of the centre-of-mass energy.

This analysis is independent from analysis I apart from the common requirement of the charged particle counting and of the use of the FEMC for neutral particles in the forward region.

The energy was calculated using the results of the reconstruction from each calorimeter, and using the combined calorimetry results (i.e. an algorithm to sum the energy depositions in the calorimeters) if the showers in the hadron and electromagnetic calorimeters were found to be associated. Fig. 5d displays the total calorimetric energy, E_{II}, of the events with at least 5 charged particles.

The corresponding selection efficiency was estimated from the Monte Carlo simulation and cross-checked on the real data sub-sample which was also retained by analysis I. The overall selection efficiency was found to be $(96.5 \pm 0.6)\%$. The main source of uncertainty comes from the variation of the response of the calorimeters during the data taking period. This variation also required a more restrictive selection of running conditions than analysis I, resulting in about 10% fewer selected events.

5.3. BACKGROUNDS

Backgrounds were removed by very similar methods in both analyses. The multiplicity cut removed cosmic events and Z^0 leptonic decays with the exception of a small fraction of $\tau^+\tau^-$ events. The energy cut rejected the remaining

contamination by beam–gas and most the two-photon interactions. By analysing the events originating far from the interaction point (viz. $10 < |z| < 30$ cm) the contribution from the beam–gas events was found to be less than 3 pb. The contamination by events produced in two-photon collisions was estimated from three sources: a Monte Carlo simulation including a quark-parton and a vector-meson contribution [12], a sample of measured two-photon collision events [13] and the sub-sample of selected multihadronic events with E_{I} between 12% and 18% of the centre-of-mass energy. All three event samples gave consistent results and the contamination was estimated to be (20 ± 10) pb at each centre-of-mass energy. The $\tau^+\tau^-$ background was determined to be $(0.3 \pm 0.1)\%$ using a Monte Carlo simulation performed with the event generator KORALZ [14].

5.4. COMPUTATION OF THE CROSS SECTION

The hadronic cross section was computed at each energy from the relation

$$\sigma_{\mathrm{h}}(E_{\mathrm{cm}}) = \frac{N_Z - N_{\mathrm{b}}}{\epsilon_Z L}(1 + f_{\mathrm{sm}}), \tag{2}$$

where N_Z stands for the number of selected hadronic events, N_{b} is the number of backgrounds events (viz. $\tau^+\tau^-$ and two-photon interaction events), L stands for the time integrated luminosity (eq. (1)) and ϵ_Z is the overall efficiency for hadronic events. f_{sm} is a correction factor due to the energy spread of the LEP beams. The latter has been estimated to be $(0.8 \pm 0.2) \times 10^{-3}$ [15], corresponding to a dispersion on the collision energy of (50 ± 10) MeV. The correction factor f_{sm} is proportional to the second derivative of the cross section and to the square of the energy spread. The main effect in correcting for the beam spread is to change the extracted value of Γ_Z by almost 4 MeV. The cross sections obtained with both analyses are given in table 3 for each centre-of-mass energy. The quoted errors are statistical only. There is an additional energy-independent normalisation uncertainty of 1.0% (1.1%) for analysis I (analysis II), of which 0.9% is due to the luminosity measurement and 0.4% (0.6%) is due to the determination of the selection efficiency of hadronic Z^0's. One observes that both analyses give very similar results. The cross sections obtained with smallest systematic and statistical uncertainties (analysis I) were then retained for the fits in sect. 7. The corresponding integrated luminosities are given in table 3, together with the number of selected Z^0's. The total integrated luminosity for the combined 1989 and 1990 data samples is 5.88 pb^{-1}.

For about one third of the total data sample, due to slight changes in the trigger or in the detection efficiency, the data sample selected at each centre-of-mass energy was corrected by an energy-dependent factor which varied between 0.05% and 0.50%.

TABLE 3

The cross sections for $e^+e^- \rightarrow$ hadrons, at different centre-of-mass energies, for the two analyses described in the text. The cross sections are corrected for the background and efficiency of selection. The errors are statistical only. The overall systematic error on these points is 0.4% on the total number of hadronic events selected with analysis I and 0.9% on the integrated luminosity, including the estimated theoretical uncertainty on the luminosity. This gives a total systematic error of 1.0% on the cross sections obtained with analysis I

Collision energy (GeV)	Analysis I (nb)	Analysis II (nb)	Int. lumi. (nb^{-1})	Number of Z^0 (Analysis I)
88.223	4.56 ± 0.12	4.56 ± 0.12	361.9	1602
88.277	4.64 ± 0.31		54.4	241
89.224	8.61 ± 0.16	8.64 ± 0.18	438.1	3655
89.277	9.24 ± 0.49		49.8	427
90.222	18.29 ± 0.28	18.41 ± 0.30	383.0	6777
90.276	19.17 ± 0.72		61.8	1094
91.029	28.70 ± 0.88		73.3	1987
91.225	31.04 ± 0.16	30.87 ± 0.17	2782.9	83413
91.276	30.54 ± 0.88		81.9	2392
91.529	29.49 ± 0.75		106.3	2984
92.220	21.91 ± 0.31	21.80 ± 0.32	415.4	8803
92.279	20.56 ± 0.94		39.8	785
93.221	12.77 ± 0.21	12.74 ± 0.22	460.2	5685
93.277	11.36 ± 0.54		54.2	587
94.218	7.94 ± 0.15	7.94 ± 0.17	463.5	3565
94.277	8.38 ± 0.56		35.0	280
95.035	6.07 ± 0.68		16.3	95

The collision energies given in table 3 are known with an absolute systematic uncertainty of about 20 MeV and a point-to-point uncertainty of about 5 MeV [16]. The collision energies published in ref. [1] have been corrected by -7 MeV.

6. Leptonic event selection, cross sections and forward–backward charge-asymmetries

The leptonic event selection is based on two very different approaches. In the first one, an attempt is made to separate the data into the three lepton flavours by a mixture of particle identification and event topology criteria. Care is taken to minimise the backgrounds (mainly cross-feeding between the different leptonic channels), whilst maintaining as high an efficiency as possible. In the second approach, there is no attempt to separate the data into the three flavour categories. This has the advantage that the selection is essentially only based on the reconstructed charged particle tracks, without recourse to any specific particle identification. The backgrounds due to cross-feeding between channels are eliminated.

The remainder of this section of the paper contains descriptions of the e^+e^-, $\mu^+\mu^-$ and $\tau^+\tau^-$ analyses, followed by an account of the l^+l^- (flavour-independent) analysis. Results are presented on the cross sections for each final state as a function of the e^+e^- centre-of-mass energy and on measurements of the forward–backward charge-asymmetry

$$A^l_{FB}(E_{cm}) = \frac{\sigma^l_F - \sigma^l_B}{\sigma^l_F + \sigma^l_B}. \tag{3}$$

In this expression, $\sigma^l_F(\sigma^l_B)$ is the cross section for the production of an l^- (where l is a charged lepton) with $\cos\theta > 0$ (< 0), where θ is the angle of the l^- with respect to the incident e^- direction.

The asymmetry at each centre-of-mass energy has been determined by two different methods. The "counting method" (used for all the samples) computes the asymmetry as

$$A_{FB} = \frac{N_F - N_B}{N_F + N_B}, \tag{4}$$

where N_F (N_B) are the number of events corrected for background contamination and detection inefficiencies with $\cos\theta > 0$ (< 0). The "maximum likelihood method" (used only for the $\mu^+\mu^-$ and $\tau^+\tau^-$) derives the asymmetry from a maximum likelihood fit to the angular distribution. The likelihood L is defined as

$$L = \prod_i \left(\tfrac{3}{8}(1 + \cos^2\theta_i) + A_{FB}\cos\theta_i\right) \tag{5}$$

where the product is taken over all the events selected for the asymmetry determination. The presence of QED radiative corrections distorts the angular distribution assumed above but at the present level of statistical precision these distortions have no significant effect on the results. Whereas in principle the counting method makes no assumption about the angular distribution, the maximum likelihood method gives slightly smaller statistical errors and, in the absence of charge asymmetric and forward–backward asymmetric inefficiencies, does not require efficiency corrections.

Finally, correction factors for the beam-energy spread (subsect. 5.4) have been applied to the cross sections of all final states.

6.1. $e^+e^- \to e^+e^-$

The cross section was measured both in the barrel region and the end cap region. Due to the very different characteristics in the two polar angle regions of the detector and of the Feynman graphs dominating the process, the two analyses

have been kept separate. The asymmetry has been studied in the barrel region only.

6.1.1. Cross section in the barrel region. The present analysis is an improved version of the one described in ref. [2] with a much stronger rejection of backgrounds. Events were retained if they satisfied the following selection criteria:

(i) There must be at least one electromagnetic cluster in the barrel electromagnetic calorimeter (HPC) with energy greater than $30 \times (\sqrt{s}/91.22)$ GeV and a second one with energy greater than $25 \times (\sqrt{s}/91.22)$ GeV. The clustering is performed to sum secondary photons coming from radiation in the detector material. A low-energy shower is added to a higher-energy one if its transverse energy relative to the first one is smaller than 0.2 GeV and their angular separation, as seen from the beam crossing point, is smaller than 5°.

(ii) Events with more than 4 charged particles with momentum greater than 1.5 GeV, δr less than 5 cm and $|\delta z|$ less than 5 cm (δr, δz as in sect. 5), and events with 2 charged particles in each of the two hemispheres, defined by the direction of the highest-energy cluster, are rejected. Events with 3–1 and 3–0 topologies are selected if the total electromagnetic energy is greater than 70 GeV. This requirement avoids the loss of events in which a photon has materialized, without an appreciable increase of the τ events background.

(iii) The longitudinal development of showers associated to charged particles must be compatible with that expected from an electron.

To avoid losses of events due to bad reconstruction of one shower in the HPC, events which failed the above selection criteria were accepted if they satisfied the following requirements: (a) one cluster with energy larger than $40 \times (\sqrt{s}/91.22)$ GeV must be present in the event; (b) one charged particle must be reconstructed in each hemisphere; (c) there must be no deposited energy beyond the first 1.5 interaction lengths of the hadron calorimeter associated with the charged particle in the hemisphere opposite to the most energetic electromagnetic shower.

In all the selected events, the two charged particle tracks, or the two most energetic electromagnetic clusters if the number of tracks is different from two or the angle between the existing two tracks is close to zero, are identified as the two final state electrons.

For the analysis of the events in the barrel region, events were retained for which:

(iv) the polar angles of both electrons are in the range $44° < \theta < 136°$;

(v) the acollinearity between the two electrons is smaller than 10°.

In addition, the following fiducial cuts are applied:

(vi) the azimuth of the impact point of one electron randomly selected in each event must be more than 1° away from the boundaries of the HPC modules;

(vii) the polar angle of both electrons must be more than 2° away from the $\theta = 90°$ boundary plane.

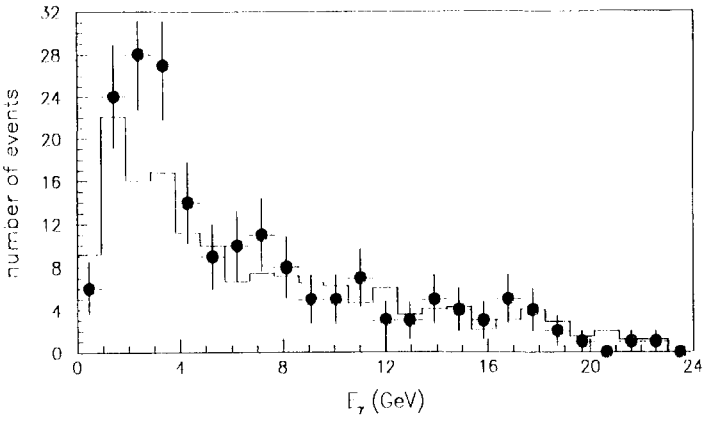

Fig. 6. The photon energy E_γ for radiative events in which the transverse energy of the photon with respect to the closest electron is larger than 0.6 GeV. The continuous line is the same distribution for simulated events. The normalisation of the two distributions is based on the relative luminosity of the two samples.

From the 1990 data a total sample of 2891 events was selected with this procedure, corresponding to an integrated luminosity of 4.35 pb^{-1}. To compute the cross section σ_c, the experimental number of events has to be corrected for trigger efficiency, losses due to the applied cuts and remaining background.

The trigger efficiency was measured to be $(99.6 \pm 0.2)\%$ by comparing the different independent subtriggers used in the experiment. To obtain the other correction factors, a sample of simulated $e^+e^-(\gamma)$ events was generated using the program BABAMC [6] and passed through the program DELSIM [17] to simulate the response of the DELPHI detector. The simulated raw data were then processed through the same analysis chain used for real data. Although the BABAMC generator contains only $O(\alpha)$ corrections, its precision is adequate for the determination of the small correction factors.

Fig. 6 compares real and simulated events with a hard radiative photon. It shows the energy distribution of the third most energetic cluster, if its transverse energy with respect to the closest more energetic cluster is larger than 0.6 GeV (in order to remove the bremsstrahlung photons produced by the passage of the electrons through the detector material). Data and simulation agree, both in shape and absolute normalisation.

For the study of background, a sample of $e^+e^- \to \tau^+\tau^-$ events was generated using the program KORALZ [14] and processed through the DELPHI simulation and analysis chain. From the study of these events the background of $e^+e^- \to \tau^+\tau^-$ events in the sample is estimated to be $(1.2 \pm 0.2)\%$. The correspondence of real and simulated τ decays has been checked using a sample of real $\tau^+\tau^-$ events, selected on the basis of cuts on one hemisphere only and therefore leaving the opposite decay unbiased.

An additional non-negligible background comes from $e^+e^- \rightarrow \gamma\gamma$ events. They can be rejected by requiring the presence of two charged particles, and by correcting for the inefficiency of the tracking system. However, since the cross section of this pure QED reaction is relatively small and well known [18], a better precision is obtained by keeping such events in the sample and correcting with the theoretical cross section. An independent analysis has however been performed using only events with two reconstructed tracks, both associated to energy clusters in the HPC. The corresponding results are fully compatible, with no indication of systematic differences.

The contamination from other sources, like $e^+e^- \rightarrow$ hadrons, was estimated to be negligible on the basis of an analysis of simulated hadronic final states.

In summary, the following correction factors were applied to the number of events at each centre-of-mass energy:

(a) 0.988 ± 0.002, at the Z^0 peak, for the residual tau pair contamination, changing with energy according to the ratio of the e^+e^- and $\tau^+\tau^-$ cross sections;

(b) 0.985 ± 0.0005 for the background due to annihilation into two photons, changing with energy according to the ratio of the cross sections for e^+e^- and $\gamma\gamma$ final states;

(c) 1.215 ± 0.007 for the loss of events. This value is the product of a factor of 1.004 ± 0.002 for the trigger efficiency and a factor of 1.210 ± 0.007, estimated using the simulated events, to correct for the cuts on the azimuthal and polar angles, the cluster energy and the longitudinal shower development. The purely geometrical component of the correction for the angular cuts is a factor of 1.206, showing that this is the most important contribution;

The cross sections computed using the 1990 data are given as function of $\sqrt{s}$ in table 4. Also given in the same table are the cross sections corrected for the effects of t-channel photon exchange and the acollinearity-angle cut and extrapolated to the full angular acceptance. The t-channel correction is calculated using the program ALIBABA [19], which computes the cross section to order α^2. The fraction of cross section due to t-channel effects is about 50% on the lowest-energy point, decreases to 13% on the peak-energy point, and it is only a few percent on the high-energy side of the resonance peak. In the event selection both electrons are required to be within the polar angle acceptance. The corresponding cross section is calculable using ALIBABA, whereas the program ZFITTER [20] only allows the polar angle of one fermion to be constrained. To make it possible to use ZFITTER to fit the pure s-channel results, a small correction, about 1%, has been applied to the cross section, calculated using ALIBABA. The correction for the acollinearity-angle cut and the extrapolation to the full angular acceptance were performed using ZFITTER.

The overall systematic error on the e^+e^- cross section coming from uncertainties on the correction factors quoted above is 0.7%, to be combined with the uncertainty on the luminosity measurement. The procedure to obtain the pure

TABLE 4

The number of selected events, integrated luminosities and cross-sections σ_e for $e^+e^- \to e^+e^-$ for different centre-of-mass energies. The fourth column ($s+t$) gives the measured cross-section within the polar-angle range $44° < \theta < 136°$ and acollinearity $< 10°$. The fifth column (s only) gives the cross section after t-channel subtraction and correction for acceptance to the full solid angle and the full acollinearity-angle distribution. The errors are statistical only. The overall systematic error on these points is 1.2%

$\sqrt{s}$ (GeV)	No. of e^+e^- events	Int. lumi. (nb^{-1})	σ_e (nb) [$s+t$]	σ_e (nb) [s only]
88.223	95	291	0.375 ± 0.042	0.275 ± 0.070
89.221	142	334	0.495 ± 0.044	0.427 ± 0.073
90.223	229	338	0.797 ± 0.054	0.895 ± 0.089
91.221	2056	2309	1.054 ± 0.024	1.497 ± 0.039
92.218	190	359	0.621 ± 0.046	1.011 ± 0.077
93.220	101	282	0.414 ± 0.043	0.698 ± 0.071
94.218	78	435	0.200 ± 0.025	0.326 ± 0.042

s-channel values introduces an additional uncertainty of 0.3% (averaged over the seven energy points), giving an overall systematic error of 1.2%.

6.1.2. Cross section in the end cap region. The selection criteria used in the end cap are similar to the ones used in the barrel region:

(i) No more than 3 charged particles with momentum greater than 1.5 GeV, δr less than 5 cm and $|\delta z|$ less than 5 cm (δr, δz as in sect. 5) must be present.

(ii) There must be at least one electromagnetic cluster in the forward electromagnetic calorimeter (FEMC) with energy greater than $30 \times (\sqrt{s}/91.22)$ GeV and a second one with energy greater than $20 \times (\sqrt{s}/91.22)$ GeV.

(iii) The polar angles of the two highest energy clusters must be in the range $10.3° < \theta < 35°$ or $145° < \theta < 169.7°$.

(iv) The acollinearity between the two clusters must be less than 10°.

In addition, a geometrical cut was applied to remove some calorimeter modules which were not working properly; they correspond to 2.0% of the cross section in the polar-angle region considered.

The trigger efficiency was measured to be $(99.9 \pm 0.1)\%$

In the present analysis, the charge of the final-state fermions is not considered and hence the scattering angles θ and $180 - \theta$ are not distinguished. The cross sections measured are therefore the sum of a forward and a backward component.

Particular care has been exercised in evaluating the losses due to the cut on the electromagnetic energy. The large amount of material between the beam crossing point and the electromagnetic calorimeter, between one and two radiation lengths on average, and its non-uniform distribution, make a detailed simulation of its effects quite difficult. To evaluate the losses, an almost pure sample of e^+e^-

events is selected by requiring an energy above 35 GeV in one end cap and a charged particle with momentum above 20 GeV, reconstructed by the forward tracking devices (TPC + FCA + FCB), in the opposite direction with an acollinearity angle smaller than 5°. The contamination in this sample from tau and hadronic events has been evaluated by Monte Carlo simulation to be smaller than 0.5%. From the tail of low energy values of the spectrum of the electromagnetic energy measured on the track side, the efficiency of the energy cuts are determined to be $(98.0 \pm 0.5)\%$. At large polar angles, due to the presence of chamber frames and a small percentage of dead counters, this value is smaller; in the region $20° < \theta < 35°$ it has been measured to be $(92.2 \pm 0.9)\%$.

From the 1990 data a total sample of 14545 events was selected with this procedure among the runs where the forward calorimeters were operational, corresponding to an integrated luminosity of 3.80 pb^{-1}. Figs. 7a–c show the differential cross section $d\sigma_e/d\nu$, where $\nu = -2/\sin^2(\theta/2)$, for events below the peak ($\sqrt{s} < 90$ GeV), near the peak ($\sqrt{s} = 90.22$ GeV and $\sqrt{s} = 91.22$ GeV) and above. With respect to the variable ν, the QED differential cross section is approximately constant. The full line curves superimposed on the data are the theoretical predictions of ref. [21]. This computation takes into account the emission of soft radiation with total energy smaller than a fraction k of the beam energy, including exponentiation, plus the emission of hard collinear photons, produced at an angle smaller than δ with respect to the final-state electrons. Since a small fraction of the cross section, corresponding to the emission of hard non-collinear photons, is not considered, the full line curves in figs. 7a–c are normalized to the data in the region $10.3° < \theta < 20°$. The normalisation factor depends on the choice of parameters k and δ. Using $k = 0.10$ and $\delta = 5°$ the factor is 1.04.

On the same figures the theoretical predictions of ref. [21] for pure photon-exchanges, without Z^0 contributions, are also shown with a dashed line. The comparison of full and dashed line curves shows that the Z^0 presence is important in the peak region for $\nu > -70$, or $\theta > 20°$. Since a complete second-order computation of the differential distributions is not yet available, for the determination of the e^+e^- partial width the analysis is restricted to the interval $20° < \theta < 35°$ and $145° < \theta < 160°$, where the contribution of s-channel exchange is of the order of 30% at the peak. In this interval, using the cuts described above, 2772 events remain.

The contamination from $e^+e^- \to \tau^+\tau^-$ and $e^+e^- \to$ hadrons in this θ region is estimated from Monte Carlo simulations to be $(1.0 \pm 0.3)\%$ at the peak. The measurement of losses due to the energy cuts has been described above. As in the barrel region, the $e^+e^- \to \gamma\gamma$ events, about 1.7% of the total in the Z^0 peak region, were kept in the sample, and a corresponding correction applied in the cross section computation.

Table 5 contains the measured cross section as a function of c.m. energy. The

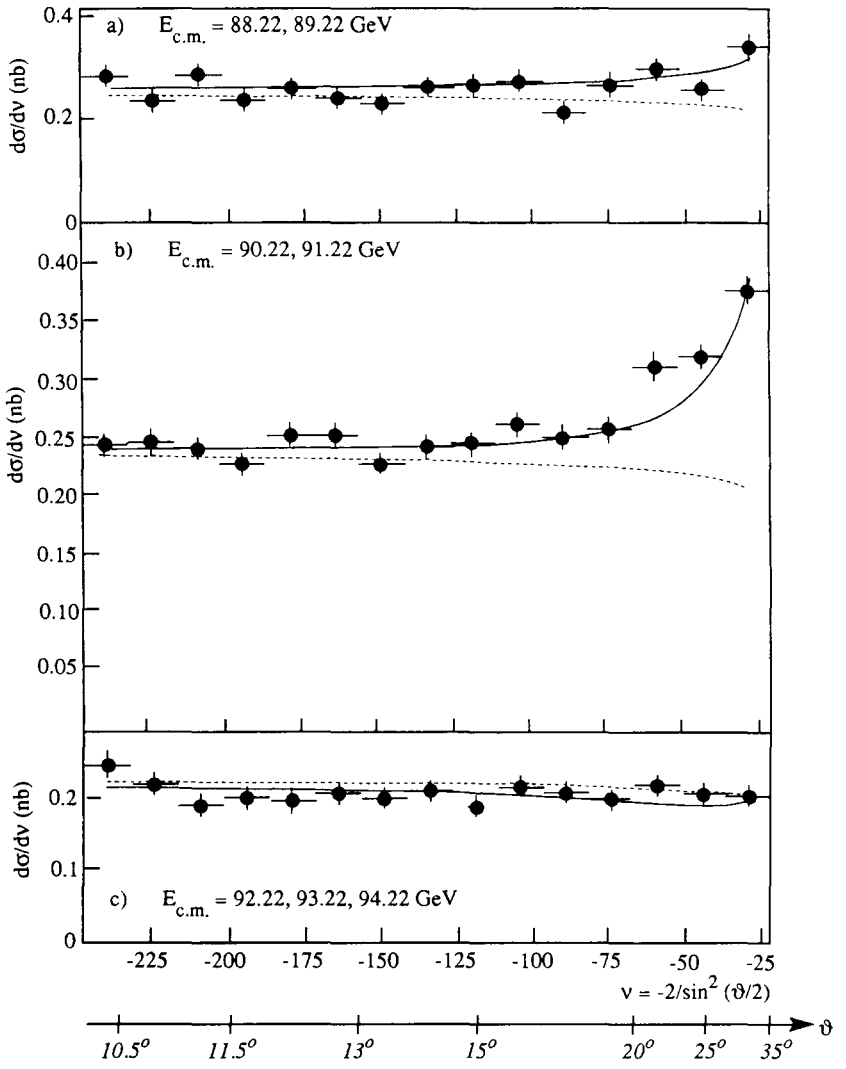

Fig. 7. $d\sigma_c/d\nu$, where $\nu = -2/\sin^2(\theta/2)$, for (a) $\sqrt{s}$ = 88.22 and 89.22 GeV (b) $\sqrt{s}$ = 90.22 and 91.22 GeV (c) $\sqrt{s}$ = 92.22, 93.22 and 94.22 GeV. The full curves are the predictions of ref. [21], normalized as described in the text. The dashed curves are the prediction from the same reference for photon exchange only.

overall systematic error on the cross section, including the luminosity uncertainty, is 1.4%.

6.1.3. Forward–backward asymmetry. The sample of events used for the cross section measurement in the barrel region has also been used to measure the forward–backward asymmetry A_{FB}. The data from the end cap region were not used because of the large t-channel contribution.

TABLE 5
The number of selected events and cross sections σ_e for $e^+e^- \to e^+e^-$ for different centre-of-mass energies within the polar-angle range $20° < \theta < 35°$ plus the symmetric interval $145° < \theta < 160°$. The errors are statistical only. The corresponding integrated luminosity is 3.8 pb^{-1}. The overall systematic error on these points, including the luminosity uncertainty, is 1.4%

$\sqrt{s}$ (GeV)	No. of e^+e^- events	Int. lumi. (nb^{-1})	σ_e (nb) $[s+t]$
88.221	219	285	0.880 ± 0.056
89.221	215	294	0.844 ± 0.054
90.218	278	311	1.026 ± 0.058
91.223	1680	2161	0.892 ± 0.020
92.221	77	131	0.673 ± 0.073
93.224	199	374	0.605 ± 0.041
94.219	104	243	0.485 ± 0.045

Two methods of measuring the charge of the electrons are available. The first one is based on the reconstruction of the charged particle trajectories in the tracking devices; the second is based on the difference in azimuthal angle ϕ of the two most energetic electromagnetic clusters of the event. Due to the bending of the electrons in the magnetic field, $\Delta\phi$ peaks at 181.1° and 178.9°, depending on

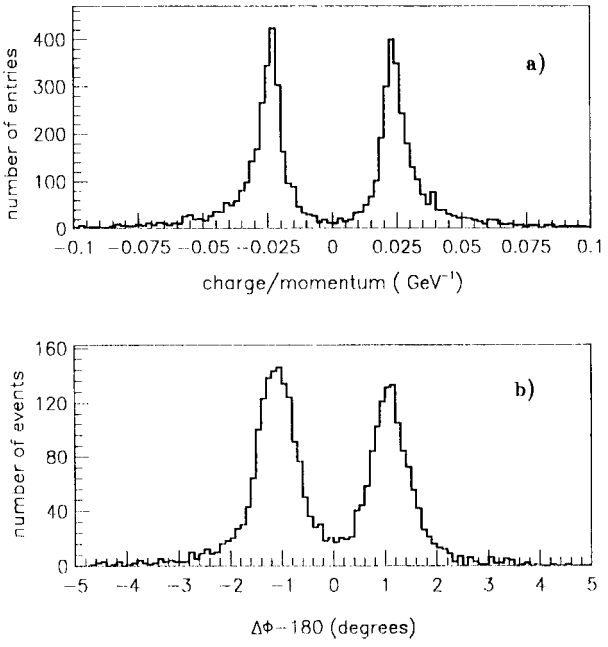

Fig. 8. (a) Distribution of the electric charge multiplied by the inverse momentum of the charged particles for $e^+e^- \to e^+e^-$ events selected in the barrel region. (b) Difference $\Delta\phi$ in the azimuthal position of the impact points on the HPC of the two maximum energy electromagnetic clusters for $e^+e^- \to e^+e^-$ events selected in the barrel region.

the charge. Fig. 8a shows the distribution of the electric charge multiplied by the inverse momentum of the charged particles of the events with two tracks. Fig. 8b shows the distribution of $\Delta\phi$ for all events with at least one reconstructed track.

An indication of the quality of the track measurement is given by the number of events with two charged particles of the same sign: 4.2% of the two track events. An important cause of wrong charge assignment in the e^+e^- final state is bremsstrahlung in the detector material, which is confirmed by the observation that in the $e^+e^- \to \mu^+\mu^-$ events the fraction is much smaller (see subsect. 6.2.2). The correlation of such an error between the two particles of an event is small, and the probability to have events with both particles wrongly assigned is about 0.1%. It should be noted that the polar and azimuthal angular distributions of wrong-charge events are uniform.

The sample of events with two charged particles of opposite sign can be used for a quantitative estimate of charge misassignment using the $\Delta\phi$ method. Amongst the events with two good tracks, $4.0 \pm 0.6\%$ ($5.1 \pm 0.7\%$) of those declared to be forward (backward) scattering events by the tracking method receive an opposite assignment from the calorimeter. Using the $\Delta\phi$ method alone, the systematic error on the asymmetry would be 9% of its value, i.e. about one third of the statistical error. Since the $\Delta\phi$ distributions of the two track events and of the remaining events are very similar, the estimate of the precision of the $\Delta\phi$ method has been assumed valid for the full sample.

The charge assignment is optimized using the tracking information for events with two charged particles of opposite charge and the calorimeter information for the remaining events. Table 6 gives the measured forward–backward asymmetries A_{FB} at all energies. The effect of the small symmetric component of $e^+e^- \to \gamma\gamma(\gamma)$ events has been taken into account. The systematic error on the asymmetry measurement due to the charge misassignment is estimated to be 0.003. The effect

TABLE 6

Results of measurements of the e^+e^- forward–backward asymmetry A_{FB} for different centre-of-mass energies. The third column ($s + t$) gives the measured asymmetry within the polar-angle range $44° < \theta < 136°$ and acollinearity $< 10°$. The fourth column (s only) gives the asymmetry after subtraction of the t-channel contribution in the same angular interval. The errors are statistical only and the data are not corrected for any of the kinematical cuts. The overall systematic error on these points is 0.005

$\sqrt{s}$ (GeV)	No. of e^+e^- events	$A_{FB}[s+t]$	$A_{FB}^s[s \text{ only}]$
88.223	95	0.46 ± 0.10	-0.03 ± 0.27
89.221	142	0.22 ± 0.08	-0.34 ± 0.19
90.223	229	0.18 ± 0.07	-0.12 ± 0.10
91.221	2056	0.067 ± 0.022	-0.046 ± 0.026
92.218	190	0.06 ± 0.08	0.05 ± 0.08
93.220	101	0.26 ± 0.10	0.26 ± 0.10
94.218	78	0.20 ± 0.12	0.16 ± 0.12

of biases in the measurement of the polar angle is negligible because both particles are required to remain within the polar angle cut. Using only the $\Delta\phi$ method for the full sample, the average change in the measured asymmetry is 0.003. No systematic effects were observed in the simulated data.

Using the program ALIBABA [19], one can correct for the effects of t-channel exchanges plus the interference with s-channel diagrams. This procedure introduces an error depending mostly on the precision of the luminosity measurement and on the accuracy of the theoretical formulae. At the level of precision of the present data this error is negligible.

The pure s-channel asymmetry, A_{FB}^{s}, corrected to one lepton in the angular region $44^\circ < \theta < 136^\circ$ (see subsect. 6.1.1) is shown in the last column of table 6. The overall systematic error on these measurements is estimated to be 0.005.

6.2. $e^+e^- \to \mu^+\mu^-$

The analysis procedure for the selection of candidate $e^+e^- \to \mu^+\mu^-$ events in the barrel region is similar to that presented in refs. [2] and [22]. In the present analysis the polar-angle range for the determination of cross sections has been further increased to $32.9^\circ < \theta < 147.1^\circ$ ($|\cos\theta| < 0.84$). For the determination of the forward–backward asymmetry the polar-angle range has been further extended to $15^\circ < \theta < 165^\circ$. This larger angular acceptance for the asymmetry measurements is important as the size of the error is related to the maximum absolute value of $\cos\theta$ in the data sample.

Events were retained if they satisfied the following selection criteria:

(i) There were two charged particles, both having momenta greater than 15 GeV, and coming from the interaction region. This region is defined by $|\delta z|$ less than 4.5 cm and δr less than 1.5 cm, where δz and δr are as defined in sect. 5.

(ii) The acollinearity angle between the two charged particle tracks was required to be less than 10°.

(iii) There were no additional charged particles with momenta greater than 5 GeV.

The momentum resolution on the reconstructed tracks used in this analysis can be seen in the distribution of the electric charge multiplied by the inverse of the momentum (fig. 9). The tails of the momentum distribution at small values of the inverse momentum are mainly due to reconstructed tracks in which information from one or more of the tracking detectors was not available in the track fit. Nevertheless this figure clearly demonstrates that the sign of the electric charge of the muons can be measured reliably, thus making possible a determination of the forward–backward asymmetry.

Five sub-detectors were used in the muon identification:

(a) For the MUB and MUF, identification was based on the association of the positions of the muon chamber hits with those expected from the extrapolation of the tracks.

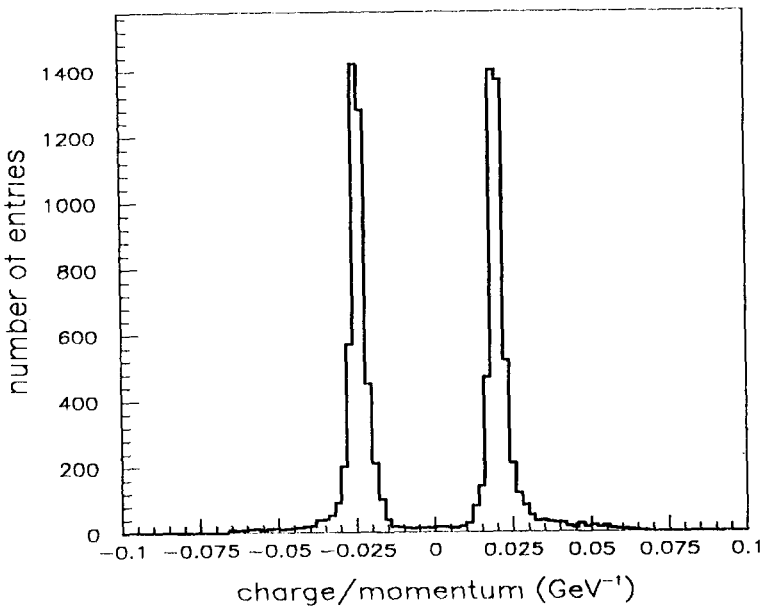

Fig. 9. The distribution of the electric charge multiplied by the inverse momentum for reconstructed tracks in the polar angle range $15° < \theta < 165°$ and used in the $e^+e^- \to \mu^+\mu^-$ analysis of the forward–backward asymmetry.

(b) For the HCAL, it was required that the energy deposited was consistent with that expected for a minimum ionising particle; namely that the total energy deposited was less than a cut-off value (which was 10 GeV at $\theta = 90°$ and increasing to about 15 GeV at $\theta = 55°$, and thereafter independent of θ) and that there were energy deposits in at least two of the four layers.

(c) For the HPC and FEMC it was required that there were energy depositions and that these were consistent with those expected from a minimum ionising particle (i.e. less than 1 GeV within $\pm 5°$ in theta and $\pm 10°$ in azimuth around the track extrapolated to the entry point of the calorimeter).

It was required that each particle was identified as a muon by at least one of the sub-detectors mentioned above in either the barrel or forward regions. Events in which one or both particles was identified as a hadron by HCAL (deposited energy greater than the above cut-off value) or in which both particles were associated with energy deposits greater than 10 GeV in the HPC or FEMC, and which had an acollinearity angle greater than 1° were removed. The cosmic ray background was substantially reduced by timing measurements using both the TOF and the OD.

The identification efficiency of each of the sub-detectors was measured using the data by counting the number of muon pairs found by a given sub-detector in a sample defined by the other two sub-detectors. The identification efficiencies were estimated as a function of θ. From these studies it was found that the overall muon

identification efficiency, which is the "or" of the sub-detector efficiencies, was 0.994 ± 0.002 over the θ range $32.9° < \theta < 147.1°$. A more restrictive cut on the acollinearity angle was made for the determination of the muon identification efficiency, in order to minimise the effect of the τ-background.

The detection efficiencies and the validity of the method of the efficiency determination were cross-checked by generating a sample of $\mu^+\mu^-$ events using the DYMU3 generator [10] and passing the simulated raw data from the DELPHI detector simulation program [17] through the same analysis chain as for the real data. Simulated events for the $\tau^+\tau^-$ final state, produced using the KORALZ generator [14], were also analysed for background studies.

6.2.1. Cross section. The cross section for $e^+e^- \to \mu^+\mu^-$ has been determined for the sample of events in which the positive muon was in the polar angle region $32.9° < \theta < 147.1°$. It was required that the sub-detector components used in the analysis were fully operational. The number of muon-pair events in this sample is 3428. The total integrated luminosity used for the determination of the cross section is 4.51 pb^{-1}.

In order to determine the cross section σ_μ the number of events at each energy was corrected for the efficiency of muon identification and by the following factors:

(i) 1.088 ± 0.004, for loss of muons, either from the dead space of the TPC or in the forward region. The efficiencies were determined using both the data and Monte Carlo simulated events. The error on this correction includes that arising from imprecision on the cuts on the vertex, on momenta and on the polar angle θ.

(ii) 1.036 ± 0.003 for trigger efficiency; this was determined by comparing which triggers fired, on an event by event basis, from a redundant set of triggers based on the ID, TPC and OD track detectors and the TOF detector in the barrel region and, in addition, FCA, FCB, HOF and MUF in the forward region.

(iii) 0.981 ± 0.005, for the $\tau^+\tau^-$ background; this was estimated from Monte Carlo simulations as described above.

(iv) 0.985 ± 0.003, for the residual cosmic ray background.

The background from the process $e^+e^- \to e^+e^-\mu^+\mu^-$, where the final state e^+ and e^- remain undetected, has been estimated using the event generator described in ref. [23]. This background, together with that from $e^+e^- \to e^+e^-$, is found to be negligible.

The cross section for $e^+e^- \to \mu^+\mu^-$, as a function of the centre-of-mass energy is given in table 7. The results are corrected for the cuts on momenta, acollinearity and polar angles, and correspond to the full 4π solid angle. The correction factors are computed using the formulae of ref. [20]. The estimated uncertainty on this calculation is 0.2%, and this is added quadratically to the above errors to give a total systematic error on the cross section of 0.8%, in addition to the error on the luminosity, or an overall systematic error of 1.2%.

TABLE 7
The number of selected events, integrated luminosities and cross sections σ_μ for $e^+e^- \to \mu^+\mu^-$ for different centre-of-mass energies. The cross sections are corrected for the cuts on momenta and acollinearity angles and to the full solid angle. The errors are statistical only. The overall systematic error on these points, including the luminosity uncertainty, is 1.2%

$\sqrt{s}$ (GeV)	No. of $\mu^+\mu^-$ events	Int. lumi. (nb^{-1})	σ_μ (nb)
88.222	49	316	0.219 ± 0.032
89.220	119	401	0.432 ± 0.040
90.223	276	374	1.090 ± 0.065
91.221	2457	2330	1.537 ± 0.031
92.218	252	307	1.177 ± 0.074
93.223	155	372	0.598 ± 0.048
94.217	120	413	0.412 ± 0.038

6.2.2. Forward–backward asymmetry. For this analysis it was required that there was at least one muon in the polar angle region $15° < \theta < 165°$. The absolute detection efficiency has not been determined for the extended parts of this polar angle region, however only the relative detection efficiency as a function of angle is required for the forward–backward asymmetry and the inclusion of this region increases the precision significantly. The other selection criteria are the same as those described above, except that a less restrictive set of data-taking runs was used since an absolute normalisation is not required. The resulting sample contained 4763 events. In this sample there are 47 apparently like-sign positive muon-pair events and 37 negative pairs. For these events the charge assignment was based on the charge of the particle with the smaller momentum error. The relative muon detection efficiency $\epsilon_\mu(|\cos\theta|)$ was determined by comparing the number of events found as a function of $|\cos\theta|$ with the distribution $(1 + \cos^2\theta)$. This function was then used to compute the factor by which the measured value of the forward–backward asymmetry, using the counting method, should be corrected to correspond to the full 4π angular range. The forward–backward asymmetry was also computed using the maximum likelihood method based on the scattering angle of the negative muon. The resulting values obtained by both methods, as a function of $\sqrt{s}$, are given in table 8. The errors shown are statistical only. The values of A_{FB} are not corrected for the momenta and acollinearity cuts. The results are in agreement with those from a previous determination based on the counting method with a smaller sample [22].

Possible systematic uncertainties on A_{FB} can arise from several sources: the wrong assignments of the charges of the particles; differences in the detection efficiencies of positive and negative particles in the forward and backward hemispheres; or in systematic differences in the momentum or polar angle values determined for positive and negative particles in the forward and backward

TABLE 8
Results of measurements of the $\mu^+\mu^-$ forward–backward asymmetry A_{FB} for different centre-of-mass energies. The results are corrected to the full solid angle, but not for the cuts on momenta and acollinearity. The errors are statistical only. The overall systematic error on these points is 0.005

$\sqrt{s}$ (GeV)	No. of $\mu^+\mu^-$ events	A_{FB} counting	A_{FB} likelihood
88.222	72	-0.23 ± 0.11	-0.14 ± 0.11
89.220	162	-0.17 ± 0.08	-0.21 ± 0.08
90.223	325	-0.11 ± 0.06	-0.08 ± 0.05
91.221	3437	0.024 ± 0.017	0.007 ± 0.017
92.218	387	0.04 ± 0.05	0.01 ± 0.05
93.223	217	0.15 ± 0.07	0.12 ± 0.07
94.217	163	0.25 ± 0.08	0.21 ± 0.08

hemispheres. From a series of studies into the above effects, the systematic error on the asymmetry is estimated to be 0.005.

6.3. $e^+e^- \to \tau^+\tau^-$

A previous study of the $e^+e^- \to \tau^+\tau^-$ channel by the DELPHI collaboration can be found in ref. [2]. The present analysis, corresponding to an integrated luminosity of 4.76 pb^{-1}, extends the polar-angle range to the region $43° < \theta < 137°$ and improves the background rejection.

The event selection criteria consisted of a combination of topological cuts based on the charged particle tracking and cuts using electromagnetic calorimetry in order to separate the $\tau^+\tau^-$ signal from the different backgrounds. These cuts are outlined below:

(i) Only charged particles with momentum greater than 1 GeV originating from a fiducial zone around the reconstructed event vertex were considered. This zone was defined by $|\delta z|$ less than 2.5 cm and δr less than 1.5 cm, where δz and δr are as defined in sect. 5.

(ii) The background from hadronic events in the sample was minimised by demanding a maximum of 6 charged particles, one of which had to be isolated in angle from all the other charged particles in the event by at least 155° and be in the polar angle range $43° < \theta < 137°$. If there was only one charged particle in the hemisphere opposite the isolated particle (i.e. the 1–1 topology), it had also to lie in this polar angle range. When there was more than one charged particle in the opposite hemisphere (i.e. the 1–N topology), there was no restriction on polar angle for these particles.

(iii) In order to minimise the contamination of events from the reaction $e^+e^- \to e^+e^-f\bar{f}$, it was required that: (a) the total visible energy in the event be greater than 8 GeV; (b) the missing transverse momentum $|\boldsymbol{P}_{\mathrm{Tmiss}}|$ be greater

than 0.4 GeV, where $\boldsymbol{P}_{\mathrm{Tmiss}}$ is defined as the vector sum of the momenta transverse to the beam direction.

(iv) In order to reduce $e^+e^- \to e^+e^-$ contamination, two cuts were made using the electromagnetic calorimetry. Events were accepted if: (a) the "radial" associated electromagnetic energy E_{rad} had to be less than 40 GeV, where $E_{\mathrm{rad}} = \sqrt{E_1^2 + E_2^2}$, E_1 is the electromagnetic energy associated with the isolated charged particle and E_2 is the total electromagnetic energy associated with the charged particles in the hemisphere opposite the isolated particle; (b) the total electromagnetic energy in the event had to be less than 70 GeV.

(v) The background due to the $e^+e^- \to \mu^+\mu^-$ channel was removed by topology dependent cuts on charged particles momenta: (a) for events of the 1–N topology where $N \geq 2$, it was required that the total visible momentum of charged particles be less than 75 GeV; (b) for events of the 1–1 topology, where this background was greater, a tighter cut was made. It was required that the "radial" momentum, P_{rad}, be less than 42 GeV, where $P_{\mathrm{rad}} = \sqrt{P_1^2 + P_2^2}$, P_1 and P_2 being the momenta of the two charged particles.

(vi) For events with 1–1 topology it was required that the acollinearity angle be greater than 0.5°. This removed any cosmic rays left in the sample.

This selection procedure gave a total of 2345 events.

The selection efficiency was determined from simulated raw data produced using KORALZ [14], with corrections for small discrepancies between observed and simulated particle losses in dead regions of the tracking detectors. On the Z^0 peak the efficiency was $(69.9 \pm 0.4)\%$ in the angular region $43° < \theta < 137°$, and varied by up to 1.2% in the energy points furthest from the peak. The quoted error on the efficiency is statistical only.

The systematic uncertainty in the selection procedure was estimated by investigating the stability of the final cross section as a function of the cuts, where the cuts were varied by amounts corresponding to the expected resolution in the cut variable. This gave an estimated fractional systematic error on the selection efficiency of 0.7%. The sensitivity of the selection efficiency to the uncertainties in the branching ratios of the different tau decay modes was found to be 0.4%. This arose primarily from the uncertainty in the branching fractions to channels containing three charged particles coupled to the isolated track requirement in cut (ii) and also the topology dependent cuts (v) and (vi). Thus, combining the statistical and systematic uncertainties in quadrature, a selection efficiency at the Z^0 peak of $(69.9 \pm 0.7)\%$ within the polar-angle acceptance was obtained.

To simulate the backgrounds, events were generated using DYMU3 [10] for the $\mu^+\mu^-$ channel, BABAMC [6] for the e^+e^- channel, LUND 7.2 [11] for the $q\bar{q}$ channel, and Berends–Daverveldt–Kleiss [24] for two-photon processes.

Simulated events were used to determine the background from $e^+e^- \to e^+e^-$ to be $(0.8 \pm 0.4)\%$. A cross-check was performed on the Monte Carlo calculated e^+e^- background using real data. Collinear e^+e^- events were selected by de-

manding a 1–1 topology with acollinearity less than 0.5°, where both charged particles lay in the polar-angle region $52° < \theta < 128°$ (defined by the polar-angle range of the barrel muon chambers), and had no associated muon chamber hits. The behaviour of the variables used in cuts (iv) and (v) described above was investigated. The number of events passing the cuts (iv) and (v) was compatible with Monte Carlo estimates. A similar procedure was carried out to select $\mu^+\mu^-$ events and the effect of cut (v) investigated. This showed that there were more $\mu^+\mu^-$ events in the region P_{rad} less than 42 GeV than predicted by Monte Carlo. The Monte Carlo predicted number for the background was corrected to account for this difference assuming that the contamination in the region P_{rad} less than 42 GeV can be simply scaled for the number of $\mu^+\mu^-$ events expected to have acollinearity $> 0.5°$. The background thus calculated was $(0.5 \pm 0.2)\%$.

The background from $e^+e^- \to q\bar{q}$ was estimated by Monte Carlo to be $(0.5^{+0.5}_{-0.3})\%$. The error was estimated from the difference between the observed events and the Monte Carlo simulation in the high-multiplicity region where this background dominated.

The contribution from the two-photon process was estimated from Monte Carlo to be (2.9 ± 1.2) pb, where the uncertainty was taken from the discrepancy between data and Monte Carlo for isolation angles less than 155°. The background due to beam–gas events and residual cosmics was estimated to be less than 0.1% from the distribution of event vertices.

Fig. 10a shows the observed isolation angle distribution and fig. 10b shows the observed multiplicity distribution, superimposed on that expected from Monte Carlo simulation, including the estimated background. In each of these plots, all other selection cuts have been applied, except the cut on the displayed variable.

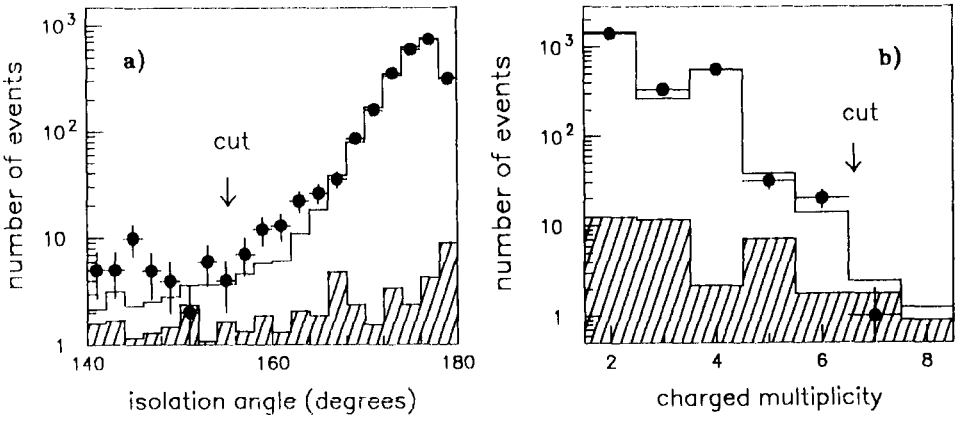

Fig. 10. For events selected in the $e^+e^- \to \tau^+\tau^-$ analysis: (a) the observed isolation angle distribution superimposed upon the Monte Carlo prediction (solid line) and the estimated background (hatched area); (b) the observed charged track multiplicity distribution superimposed upon the Monte Carlo prediction (solid line) and the estimated background (hatched area). The cut on each of these variables used in the analysis is indicated with an arrow.

TABLE 9
The number of selected events, integrated luminosities and cross sections σ_τ for $e^+e^- \to \tau^+\tau^-$ for different centre-of-mass energies, corrected to the 4π solid angle. Only statistical errors are quoted. The overall systematic error on these points, including the luminosity uncertainty, is 1.5%

$\sqrt{s}$ (GeV)	No. of $\tau^+\tau^-$ events	Int. lumi. (nb^{-1})	σ_τ (nb)
88.222	33	322	0.221 ± 0.039
89.220	76	358	0.461 ± 0.053
90.218	164	369	0.981 ± 0.076
91.222	1738	2556	1.481 ± 0.036
92.219	170	385	0.950 ± 0.074
93.221	88	315	0.601 ± 0.065
94.218	76	452	0.364 ± 0.042

6.3.1. Cross section. In order to determine the cross section in the full solid angle, the number of events at each energy, after correction for the two-photon background, was multiplied by the following factors:

(i) 0.982 ± 0.006 for background from hadronic and non-tau leptonic decays of the Z^0.

(ii) 1.005 ± 0.002 for the trigger efficiency.

(iii) 2.214 ± 0.022 for the selection cuts on the Z^0 peak point, and slightly different factors for the other points. This includes corrections for acceptance, kinematic cuts and particle losses in dead regions of the tracking detectors.

The fully corrected cross-section values as a function of centre-of-mass energy are given in table 9. The overall systematic error is 1.2% excluding the 0.9% error from the luminosity measurements.

6.3.2. Forward–backward asymmetry. The same data sample was used to calculate the forward–backward asymmetry. Table 10 gives the values of the asymmetries calculated by the method (corrected for acceptance to the full solid angle) and by the maximum likelihood method, for the seven centre-of-mass-energies.

TABLE 10
Results of measurements of the $\tau^+\tau^-$ forward–backward asymmetry A_{FB} for different centre-of-mass energies. The results are corrected to the full solid angle, but not for the cuts on momenta and acollinearity. The errors are statistical only. The overall systematic error on these points is 0.005

$\sqrt{s}$ (GeV)	No of $\tau^+\tau^-$ events	A_{FB} counting	A_{FB} likelihood
88.222	33	-0.33 ± 0.20	-0.30 ± 0.18
89.220	76	0.05 ± 0.14	0.00 ± 0.13
90.218	164	-0.15 ± 0.09	-0.12 ± 0.08
91.222	1738	-0.011 ± 0.029	-0.014 ± 0.026
92.219	170	0.04 ± 0.09	0.04 ± 0.08
93.221	88	-0.05 ± 0.13	0.03 ± 0.12
94.218	76	-0.08 ± 0.14	0.06 ± 0.14

For this study the positively charged particle was used in 1–1 events and in events with a 1–N topology the measured charge of only the isolated particle was used.

A source of systematic error arises from the possible wrong assignment of the particle charge. Only 0.3% of events of the 1–1 topology had like-sign particles, implying that only 0.15% of particles had their charge incorrectly determined. To perform a consistency check with the observed events, a comparison was made in which the asymmetry was calculated using only events for which the net electric charge of all the particles was zero. A study of the effect of the tau decay product direction at the edges of the experimental fiducial zones and in the $\theta = 90°$ boundary zone was made using Monte Carlo events. The overall systematic error on the asymmetry due to the above effects was estimated to be 0.005.

6.4. $e^+e^- \to l^+l^-$

In this analysis the leptonic decays $Z^0 \to l^+l^-$ (where $l = e, \mu, \tau$) were selected without trying to separate the three flavours. Once universality is assumed, this approach has several advantageous features. It allows a very efficient selection of leptonic events, since no tight cuts are needed to separate the different families. Since a leptonic event has a very clean signature that separates it from potential backgrounds (hadronic events, two-photon events, etc.) low levels of contaminations are expected (recall that the leptonic channels are the main background to one another). In addition, an analysis independent of lepton flavour can be based primarily on the selection of the reconstructed charged particle tracks. Therefore, this and the flavour dependent leptonic analysis provide a powerful consistency check of one another.

Although the event selection is independent of lepton flavour, and the trigger and event selection efficiencies are derived likewise, the e^+e^-, $\mu^+\mu^-$ and $\tau^+\tau^-$ fractions of the sample have to be determined in order to compute the $e^+e^- \to e^+e^-$ t-channel contribution. Since only the tracking detectors were used to select the events, the electromagnetic and hadronic calorimeters, as well as the muon chambers, can be used to select a very pure sample of e^+e^- and $\mu^+\mu^-$ events in order to estimate the selection efficiency of these channels directly from the data. As it is very difficult to select the $\tau^+\tau^-$ events without using the tracking detectors, the efficiency for the $\tau^+\tau^-$ component of the sample was estimated by simulation.

The event selection takes advantage of the distinctive features of a leptonic event: low multiplicity, back-to-back topology and high visible momentum. It was restricted to the barrel region covering the angular range $43° < \theta < 137°$. Events were retained if they satisfied the following selection criteria:

(i) There were between 2 and 6 charged particles with momentum greater than 0.2 GeV, produced near the interaction region, i.e. with $|\delta z|$ less than 10.0 cm, δr less than 5.0 cm, where δz and δr are defined in sect. 5. The charged-multiplicity

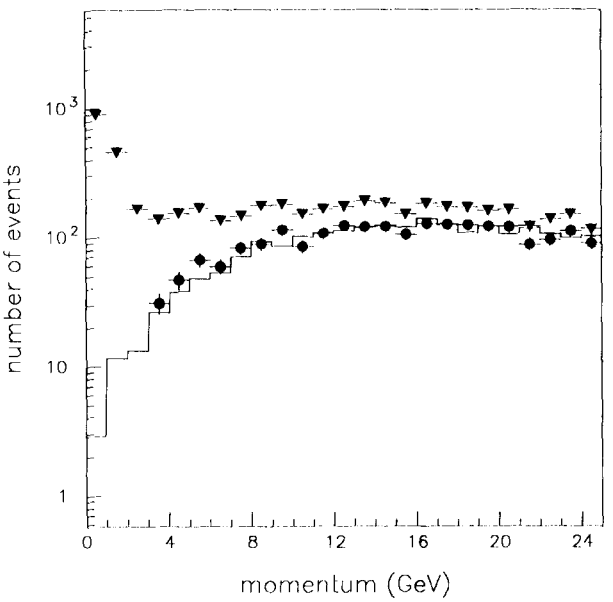

Fig. 11. Momentum distribution for the highest-momentum charged particle in low multiplicity events (< 9 charged particles) selected in the flavour-independent analysis of $e^+e^- \to l^+l^-$. The triangles correspond to the measured events after the multiplicity cut only. The dots correspond to the selected events after all cuts and the solid line is the Monte Carlo simulation prediction without cuts.

cut by itself is enough to suppress most of the hadronic background, as illustrated in fig. 5a, where the charged-multiplicity distribution is shown for the data sample used for the hadronic analysis (using very similar track-selection criteria).

(ii) Dividing the event into two hemispheres by a plane perpendicular to the thrust axis, one of the hemispheres was required to have a single charged particle with transverse momentum (with respect to the beam axis) greater than 1.5 GeV. The other hemisphere could have from 1 to 5 charged particles.

(iii) The event acollinearity angle was required to be less than 20°. For events with more than one charged particle in a hemisphere, the acollinearity angle is the angle between the isolated particle and the resultant momentum of the particles in the other hemisphere.

(iv) The opening angle between any track in the jet and the resultant momentum was required to be less than 30°.

(v) In order to suppress the low-energy background events arising from beam–gas, beam–wall and two-photon interactions, it was demanded that at least one charged particle in the event had momentum greater than 3 GeV. The effectiveness of this cut is illustrated in fig. 11 where the momentum distribution of the highest-momentum particle in each event is shown for low-multiplicity events (less than 9 charged particles). Note the fast rise of the distribution for momentum less than 2 GeV, corresponding to the backgrounds mentioned above. Only a very

small fraction (a few per mille) of the leptonic events fall below the 3 GeV momentum cut. Conversely, above 3 GeV the level of background is very small, as indicated by the very good agreement between the distribution of the measured events and the Monte Carlo simulation.

Requirements (i) to (iv) are equivalent to demanding a two-jet configuration with topology 1–N ($N = 1,5$) and an isolation angle of 150° between the isolated track and the jet.

Cosmic rays were removed by means of a tighter cut on the vertex relative to the interaction point for those events with only two selected charged particles ($\delta r < 1.5$ cm and $|\delta z| < 3$ cm), together with a cut on the time-of-flight of the particles.

A total of 10 117 events pass these selection criteria, corresponding to a total integrated luminosity of 4.97 pb^{-1}. The overall trigger efficiency in the angular region considered was found to be $(99.0 \pm 0.3)\%$.

The selection efficiency estimates rely mainly on the data. The e^+e^- events were selected using the HPC be requiring at least two back-to-back electromagnetic showers with high energy deposition (greater than 30 GeV) on each side. The $\mu^+\mu^-$ events were selected requiring a minimum ionizing particle signal in the HPC and a low energy deposition in the hadronic calorimeter and associated hits in the muon chambers. For $\tau^+\tau^-$ events a selection completely independent of the tracking detectors is very difficult. Thus, use was made on the selection described in subsect. 6.3 to cross-check the Monte Carlo calculation. The resulting combined selection efficiency, taking account of the t-channel contribution to the e^+e^- cross section, was $(91.0 \pm 0.3)\%$, which corresponds to $(92.5 \pm 0.7)\%$ for e^+e^-, $(94.0 \pm 0.5)\%$ for $\mu^+\mu^-$ and $(85.0 \pm 0.5)\%$ for $\tau^+\tau^-$. The main source of inefficiency in each channel was the loss of tracks in the azimuthal dead-zones of the TPC.

As mentioned above, the main sources of potential background were multihadronic events, cosmic rays, two-photon events and beam–gas and beam–wall interactions. The hadronic and two-photon events backgrounds were computed, using Monte Carlo, to be $(0.3 \pm 0.2)\%$ and (7 ± 1) pb respectively. The background due to cosmic events was estimated from the data to be $(0.3 \pm 0.1)\%$ at the Z^0 peak. The two-photon and cosmic backgrounds are non-resonant and require larger percentage corrections off-peak than on-peak. All the other backgrounds are found to be negligible.

6.4.1. Cross section. In order to determine the cross sections within the polar-angle acceptance, the number of events at each energy, after correction for the non-resonant backgrounds mentioned above, was multiplied by the following factors: (i) 0.997 ± 0.002 for the hadronic background. (ii) 1.010 ± 0.003 for the trigger efficiency. (iii) 1.099 ± 0.004 for the selection efficiency, excluding the acollinearity cut.

The cross section values thus obtained are given as a function of center-of-mass energy in the fourth column of table 11. These cross sections have not been

TABLE 11

The number of selected events, integrated luminosities and cross sections σ_f for $e^+e^- \to l^+l^-$ (flavour-independent analysis) for different centre-of-mass energies. The fourth column ($s+t$, 3) gives the measured cross section within the polar-angle range $43° < \theta < 137°$ and acollinearity $< 20°$. The fifth column (s only, 1) gives the cross section, reduced to one lepton generation, after t-channel subtraction and correction for acceptance to the full solid angle and the full acollinearity-angle distribution. The errors are statistical only. The overall systematic error on these points, including the luminosity uncertainty, is 1.1%

$\sqrt{s}$ (GeV)	No. of l^+l^- events	Int. lumi. (nb^{-1})	σ_f (nb) [$s+t$, 3]	σ_f (nb) [s only, 1]
88.220	173	295	0.646 ± 0.050	0.223 ± 0.017
89.221	421	408	1.134 ± 0.056	0.448 ± 0.022
90.221	749	378	2.208 ± 0.084	0.990 ± 0.037
91.220	7272	2627	3.077 ± 0.038	1.516 ± 0.019
92.220	733	388	2.088 ± 0.080	1.078 ± 0.041
93.222	436	420	1.140 ± 0.056	0.593 ± 0.029
94.217	333	458	0.794 ± 0.044	0.403 ± 0.022

corrected for the effects of the acollinearity-angle cut. In the fifth column of table 11 the cross sections are given, reduced to one lepton generation, after corrections for the acollinearity-angle cut (a multiplicative factor 1.016 ± 0.002 at the Z^0 peak, with somewhat larger values off the peak), for the effects of the $e^+e^- \to e^+e^-$ t-channel contribution and for the polar-angle acceptance. The $e^+e^- \to e^+e^-$ t-channel contribution was subtracted using the program ALIBABA [19]. This procedure introduces a 0.1% uncertainty in the cross sections. The overall systematic error is 0.6% excluding the 0.9% error from the luminosity measurements.

6.4.2. Forward–backward asymmetry. The charge asymmetry was also computed. To avoid systematic errors associated with track superposition and bad charge-determination in τ decays to more than one charged particle, only the 1–1 topology events with oppositely-charged particles were retained in this analysis. A total of 8045 events were selected. The asymmetry was computed by the counting method and corrections were applied for the cosmic ray and two-photon event backgrounds. Finally, a correction was applied to remove the effect of the $e^+e^- \to e^+e^-$ t-channel contribution, taking into account the known efficiency for selecting $e^+e^- \to e^+e^-$ events. In table 12 the values of the charge asymmetry are given. The asymmetry values before t-channel subtraction are given in the third column and the values of the pure s-channel asymmetry, A_{FB}^{s}, are in the fourth column. The main source of systematic error comes from possible misidentification of the charge, as discussed in subsects. 6.1.3, 6.2.2 and 6.3.2, and it is estimated to be 0.005.

TABLE 12
Results of measurements of the l^+l^- forward–backward asymmetry A_{FB} (flavour-independent analysis) for different centre-of-mass energies. The third column ($s+t$) gives the asymmetry within the polar angle range $43° < \theta < 137°$ and acollinearity $< 20°$. The fourth column (s only) gives the asymmetry after subtraction of the t-channel contribution in the same angular interval. The errors are statistical only and the data are not corrected for any of the kinematical cuts. The overall systematic error on these points is 0.005

$\sqrt{s}$ (GeV)	No. of l^+l^- events	$A_{FB}[s+t]$	$A_{FB}^{s}[s \text{ only}]$
88.220	141	0.19 ± 0.09	-0.20 ± 0.10
89.221	333	0.00 ± 0.05	-0.26 ± 0.06
90.221	606	0.03 ± 0.04	-0.10 ± 0.04
91.220	5774	0.041 ± 0.013	-0.001 ± 0.013
92.220	584	0.03 ± 0.04	0.02 ± 0.04
93.222	341	0.11 ± 0.05	0.11 ± 0.05
94.227	266	0.20 ± 0.06	0.17 ± 0.06

7. Extraction of the Z^0 parameters

This section describes how the Z^0 resonance parameters and the couplings of Z^0 to charged leptons were extracted from the data by fitting the experimental lineshapes and leptonic aysmmetries with theoretical formulae. An interpretation of the results within and beyond the boundaries of the Minimal Standard Model (MSM) follows (in sect. 8), where the number of light neutrino types is derived, a detailed search for deviations from the expectations of the MSM is made and, finally, lower limits are set on the masses of new particles predicted in extensions of and alternatives to the MSM. The smaller systematic uncertainties and ten-fold larger statistics of the 1990 data sample improve significantly the precision on the fit parameters determined with the 1989 data sample [1,2].

The event samples, acceptances, efficiencies, backgrounds and systematic errors in the hadronic and leptonic cross section analyses are summarized in table 13.

7.1. FORMULAE USED TO DETERMINE THE Z^0 PARAMETERS

The formulae used for the fits (contained in the program ZFITTER [20]) include the most recent calculations of electroweak corrections to the Born cross section. It is more accurate than the expression used in ref. [1] * and can be written as follows:

$$\sigma^{\text{obs}}(s) = \int_0^s \left[\sigma_W(s') F_i(s', s) + \Delta_{\text{int}}\right] \mathrm{d}s', \tag{6}$$

* Fits with the formula of ref. [26] tend to underestimate M_Z and Γ_Z by about 2 MeV and to overestimate σ_0 by approximately 0.1%.

TABLE 13
Summary of events samples, acceptances, efficiencies, backgrounds and systematic errors in the hadronic and leptonic cross section analyses

	Channel				
	Hadrons [a]	e^+e^-	$\mu^+\mu^-$	$\tau^+\tau^-$	l^+l^-
Integ. luminosity (pb^{-1})	5.88	4.35	4.51	4.76	4.97
Selected events	125000	2891	3428	2345	10117
θ acceptance (°)	0–180	44–136	33–147	43–137	43–137
Selection efficiency (%)	96.3 ± 0.4	82.6 ± 0.5	91.4 ± 0.4	69.9 ± 0.7	91.0 ± 0.3
Trigger efficiency (%)	100.0	99.6 ± 0.2	96.5 ± 0.3	99.5 ± 0.2	99.0 ± 0.3
$\tau^+\tau^-$ background (%)	0.3 ± 0.1	1.2 ± 0.2	1.9 ± 0.5	–	–
$q\bar{q}$ background (%	–	–	–	$0.5^{+0.5}_{-0.3}$	0.3 ± 0.2
$e^+e^- + \mu^+\mu^-$ bkgd. (%)	–	–	–	1.3 ± 0.4	–
Two-photon bkgd. (pb)	20 ± 10	–	–	2.9 ± 1.2	7 ± 2
Peak cosmic bkgd. (%)	–	–	0.8 ± 0.2	–	0.3 ± 0.1
Kinematic corr. error (%)	–	0.3 [b]	0.2	–	0.2
Total syst. error (%)	0.4	0.7	0.8	1.2	0.6
Syst. error on σ_T (%) [c]	1.0	1.2	1.2	1.5	1.1

[a] Ten thousand 1989 hadronic events included (0.57 pb^{-1}).
[b] Uncertainty on electron t-channel subtraction and kinematic cuts.
[c] Includes 0.9% systematic error on luminosity. The trigger and selection efficiencies refer to the quoted polar angle range for each Z^0 decay channel.

where σ_W is the Born cross section with full $O(\alpha)$ electroweak corrections [25], F_i is the initial-state pure QED radiative correction and Δ_{int} describes the interference of initial- and final-state radiation as well as QED box-diagrams; s' is the square of the invariant mass of the final-state fermions.

The dominant initial-state radiation function has the form

$$F_i(s', s) = \beta_e\left(1 - \frac{s'}{s}\right)^{\beta_e - 1}(1 + \delta_{s+v}) + \delta_h(s'), \tag{7}$$

where the first term stands for the exponentiated leading contributions of soft and hard collinear photons multiplied by the remaining soft and virtual corrections up to second order in α. The second term absorbs the remnant hard photon contribution. The expressions for β_e, δ_{s+v} and δ_h can be found in ref. [20].

The modified Born cross section σ_W for $e^+e^- \to$ hadrons can be expressed in a way convenient for an almost model-independent fit of the lineshape [25]

$$\sigma_W(s) = \left(\frac{12\pi\Gamma_e\Gamma_h}{M_Z^2}\right)\left(\frac{1}{1 + (3\alpha/4\pi)}\right)\frac{s}{(s - M_Z^2)^2 + (s^2\Gamma_Z^2/M_Z^2)}$$

$$+ (\sigma^{\gamma Z} + \sigma^{\gamma})(1 + \delta_{QCD}), \tag{8}$$

TABLE 14
Systematic errors on the hadronic and leptonic cross sections which are propagated in the fits described in the text

Source of systematic error	Error (%)
Luminosity	0.9
Hadron selection	0.4
e^+e^- selection	0.7
$\mu^+\mu^-$ selection	0.8
$\tau^+\tau^-$ selection	1.2
l^+l^- selection	0.6

where M_Z and Γ_Z are the mass and total width of the Z^0 and Γ_e and Γ_h are the electron and hadron partial widths respectively. The terms σ^γ and $\sigma^{\gamma Z}$ correspond respectively to the photon exchange and to the interference between photon and Z^0 exchange. They are corrected for final-state pure QED radiative effects and final-state gluon radiation by the function δ_{QCD}, computed up to third order in α_s within the $\overline{MS}$ scheme. The term containing α is the final-state pure QED radiative correction to the leptonic partial width, which must be present to avoid double-counting this correction in eq. (6).

The above formulae are modified in the case of leptonic decays of the Z^0 by the replacement of the hadronic partial width by the appropriate leptonic partial width and by the removal of the QCD correction term. A similar formalism, based on the improved Born approximation [20] is adopted in the case of the forward–backward charge asymmetries of the leptons. A particularly important feature of the formulae used for the leptonic asymmetry fits was the inclusion of realistic experimental cuts on several kinematic variables (polar angle, momentum and acollinearity angle).

A χ^2-minimisation procedure was adopted for the fitting of the theoretical expressions to the measurements, including a full covariance matrix treatment of the errors. The systematic errors propagated in the fits to the hadronic and leptonic lineshapes are given in table 14. The origin of these errors is described in sects. 5 and 6 of this paper. For the asymmetry fits the $\mu^+\mu^-$ and $\tau^+\tau^-$ asymmetry values determined by the maximum-likelihood method were used. The systematic error assigned to each of the leptonic channels for the asymmetry measurements is 0.005.

The endcap $e^+e^- \to e^+e^-$ cross section measurements were not used in the combined fits because the t-channel contribution was dominant in this polar-angle range and hence large uncertainties would have been introduced after the t-channel subtraction. Nevertheless, a value for the electron partial width has been obtained in a fit to these data alone and the results are presented in subsect. 7.3.2.

7.2. FIT TO THE HADRONIC LINESHAPE PARAMETERS

In order to understand the role played by the hadronic lineshape measurement in the global fits to all the data, a fit was performed just to the hadronic lineshape. In this fit, M_Z, Γ_Z and the product of the partial widths $\Gamma_e\Gamma_h$ were left free to vary in order to determine the total width without constraint from the overall normalisation of the data.

The fit gave the following results:

$$M_Z = 91.183 \pm 0.011(\text{stat.}) \pm 0.02(E_{cm}) \text{ GeV},$$

$$\Gamma_Z = 2.465 \pm 0.020(\text{stat.}) \pm 0.005(\text{syst.}) \text{ GeV},$$

$$\Gamma_e\Gamma_h = 0.1443 \pm 0.0019(\text{stat.}) \pm 0.0013(\text{syst.}) \text{ GeV}^2,$$

$$\chi^2/\text{d.o.f.} = 8.5/14.$$

The systematic error on M_Z is completely dominated by the 20 MeV error in E_{cm} due to the LEP energy calibration [16]. A systematic error of 5 MeV has been assigned to Γ_Z due to point-to-point variation in the normalisation of the cross section, variations in the LEP beam-energy setting and uncertainties in the two-photon background subtraction. The results of the fit are shown in figure 12.

The value of the unfolded Born cross section at the pole $\sigma_0 = 12\pi\Gamma_e\Gamma_h/M_Z^2\Gamma_Z^2$ corresponding to the fitted values above is

$$\sigma_0 = 41.92 \pm 0.22(\text{stat.}) \pm 0.39(\text{syst.}) \text{ nb}.$$

The systematic error on σ_0 includes a contribution of 0.21 nb coming exclusively from the uncertainty on the theoretical expression of the small-angle Bhabha cross section (see sect. 3).

The correlation between Γ_Z and σ_0 is illustrated in fig. 13 where the fitted values of both parameters are shown with their 68% and 99% confidence level contours, along with the predictions of the MSM. One observes that Γ_Z is quite sensitive to variations in m_{top} and α_s, whereas σ_0 displays much less sensitivity (see subsect. 8.1.1 for further discussion). Good agreement is observed between the measured values and the MSM predictions.

The fit was repeated with the formulation of the cross section used in the previous publication [26]. The results agree well with the values given above.

7.3. FIT TO THE HADRONIC AND LEPTONIC LINESHAPE PARAMETERS

7.3.1. Lepton universality assumed. Having observed how the hadronic lineshape tightly constraints the mass and total width of the Z^0, the next step in the analysis is to study how much the fit of these parameters is influenced by the

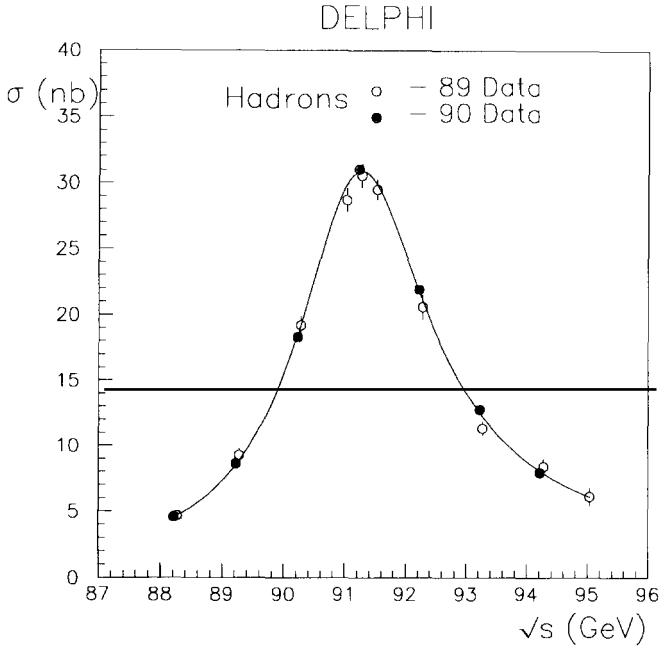

Fig. 12. Cross sections for $e^+e^- \rightarrow$ hadrons as measured at seventeen different energies. Also shown (solid line) is the result of the three-parameter fit described in the text.

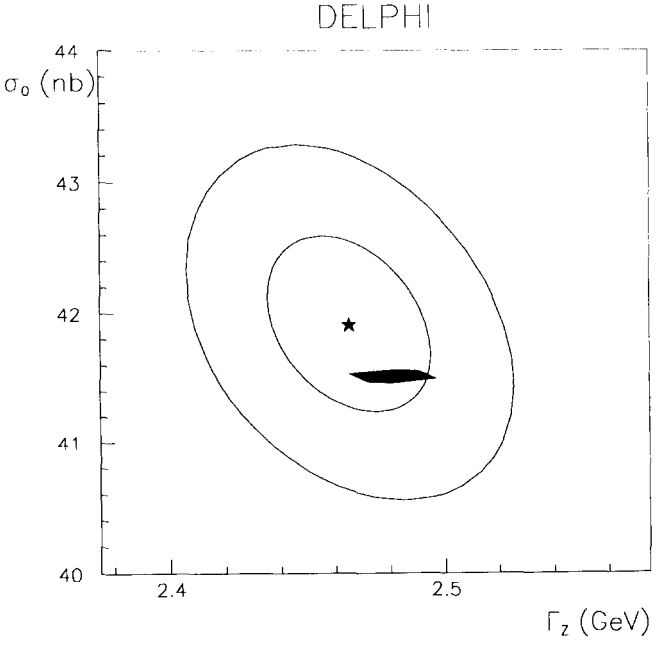

Fig. 13. The 68% and 99% confidence level contours in the Γ_Z, σ_0 plane for the three-parameter fit to the hadronic lineshape. Also shown is the MSM prediction for three massless neutrino species assuming a top-quark mass of 139 ± 38 GeV, a Higgs mass of 300 GeV, allowed to vary from 50 to 1000 GeV, and a value of α_s of 0.110 ± 0.006.

leptonic lineshapes. Furthermore, it is also possible to derive the hadronic and leptonic partial widths from the data.

A four-parameter fit applied simultaneously to the hadronic cross section and to the three leptonic cross sections determines the hadronic, leptonic and total widths in addition to the Z^0 mass, giving

$$M_Z = 91.177 \pm 0.010(\text{stat.}) \pm 0.02(E_{\text{cm}})\ \text{GeV},$$

$$\Gamma_Z = 2.465 \pm 0.019(\text{stat.}) \pm 0.005(\text{syst.})\ \text{GeV},$$

$$\Gamma_h = 1.726 \pm 0.015(\text{stat.}) \pm 0.011(\text{syst.})\ \text{GeV},$$

$$\Gamma_\ell = 83.4 \pm 0.7(\text{stat.}) \pm 0.5(\text{syst.})\ \text{MeV}$$

$$\chi^2/\text{d.o.f.} = 31/34.$$

The value of the mass of the Z^0 from this fit is only a few MeV different from the value found with the fit to the hadronic lineshape alone, and the value of the total width remains unchanged.

The results of this fit are displayed in fig. 14. The 68% and 99% confidence level contours in the Γ_h, Γ_ℓ plane are shown in fig. 15. These parameters are

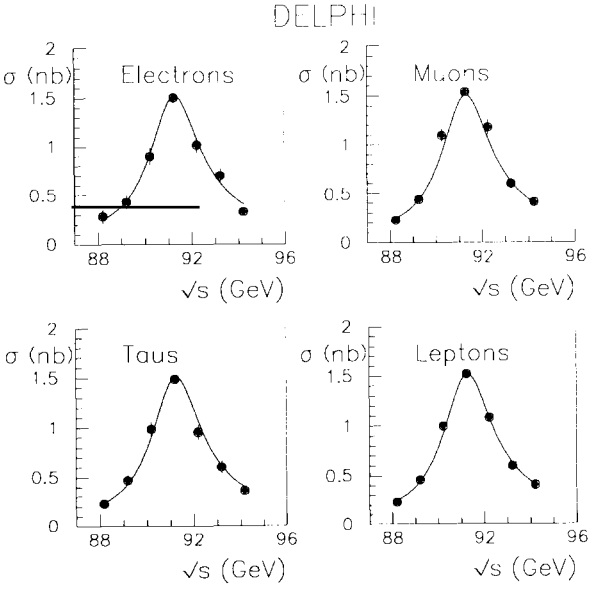

Fig. 14. Cross sections for $e^+e^- \to e^+e^-$ (t-channel subtracted), $e^+e^- \to \mu^+\mu^-$, $e^+e^- \to \tau^+\tau^-$ and $e^+e^- \to l^+l^-$ (flavour-independent analysis, electron t-channel subtracted), as a function of the centre-of-mass energy around the Z^0 pole. The cross sections are corrected for acceptance to the full solid angle. The solid curves are the results of a four-parameter combined fit to the lineshapes as described in the text.

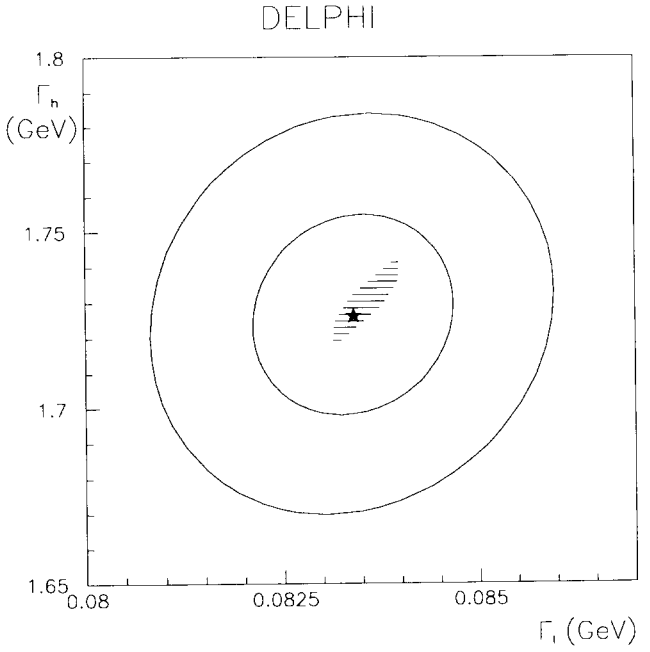

Fig. 15. The 68% and 99% confidence level contours in the Γ_h, Γ_ℓ plane for the four-parameter fit to the hadronic and leptonic lineshapes. Also shown is the MSM prediction for three massless neutrino species assuming a top-quark mass of 139 ± 38 GeV, a Higgs mass of 300 GeV, allowed to vary from 50 to 1000 GeV, and a value of α_s of 0.110 ± 0.006.

sensitive to details of the MSM, particularly the top-quark mass, and one observes how the data compare with a range of values of the top quark and the Higgs boson mass. The parameter correlation matrix for this fit is given in appendix A.

Repeating the four-parameter fit above using the flavour-independent lepton cross-sections, instead of the individual leptonic lineshapes, yields

$$M_Z = 91.177 \pm 0.010(\text{stat.}) \pm 0.02(E_{\text{cm}}) \text{ GeV},$$

$$\Gamma_Z = 2.465 \pm 0.019(\text{stat.}) \pm 0.005(\text{syst.}) \text{ GeV},$$

$$\Gamma_h = 1.723 \pm 0.015(\text{stat.}) \pm 0.011(\text{syst.}) \text{ GeV},$$

$$\Gamma_\ell = 83.7 \pm 0.7(\text{stat.}) \pm 0.5(\text{syst.}) \text{ MeV},$$

$$\chi^2/\text{d.o.f.} = 15/20.$$

The results of this fit are displayed in fig. 14. Very good agreement is found between the values of the resonance parameters obtained with this analysis and the one requiring identification of the leptonic flavour, although the event selection procedures are very different. This result is an important consistency check of the flavour-dependent analyses. In the remainder of the text, details will only be

given for fits using the flavour-separated lepton samples, although the results of the same fits using the flavour-independent lepton sample can be found in table 15.

7.3.2. Lepton universality not assumed. The flavour-separation of the leptonic sample allows an important test of lepton universality. Repeating the combined fit to the lineshapes without the assumption of leptonic universality (six-parameter fit) gave the following results:

$$M_Z = 91.177 \pm 0.010(\text{stat.}) \pm 0.02(E_{\text{cm}}) \text{ GeV},$$

$$\Gamma_Z = 2.465 \pm 0.019(\text{stat.}) \pm 0.005(\text{syst.}) \text{ GeV},$$

$$\Gamma_h = 1.747 \pm 0.023(\text{stat.}) \pm 0.012(\text{syst.}) \text{ GeV},$$

$$\Gamma_e = 82.4 \pm 1.1(\text{stat.}) \pm 0.5(\text{syst.}) \text{ MeV},$$

$$\Gamma_\mu = 86.9 \pm 1.9(\text{stat.}) \pm 0.9(\text{syst.}) \text{ MeV},$$

$$\Gamma_\tau = 82.7 \pm 2.1(\text{stat.}) \pm 1.1(\text{syst.}) \text{ MeV},$$

$$\chi^2/\text{d.o.f.} = 27/32,$$

where the Γ_e, Γ_μ and Γ_τ are the individual leptonic partial widths. Taking into account the relevant correlations, the ratio of the muon (tau) partial width to the electron partial width is 1.054 ± 0.033 (1.003 ± 0.035) and one can conclude that the data are consistent with the hypothesis of universal leptonic couplings. The parameter correlation matrix for this fit can be found in appendix A.

A one-parameter fit, using the theoretical formulae of refs. [19] and [21], to the endcap $e^+e^- \rightarrow e^+e^-$ cross sections (without t-channel subtraction), fixing M_Z and Γ_Z to the values given above, yields a value for the electron partial width

$$\Gamma_e = 83.8 \pm 2.9(\text{stat.}) \pm 2.1(\text{syst.}) \text{ MeV}$$

where the systematic error takes into account the uncertainty on the luminosity measurement, the uncertainty on Γ_Z and the uncertainty on the event selection. This result is in good agreement with the value reported above from the six-parameter fit.

7.4. THE EFFECTIVE Z^0 COUPLINGS TO CHARGED LEPTONS FROM FITS TO THE LINESHAPES AND CHARGE ASYMMETRIES

The leptonic partial width and the forward–backward charge-asymmetry at the Z^0 pole can be parameterised (Improved Born Approximation) in terms of

effective vector and axial-vector couplings ($\bar{V}_\ell$ and $\bar{A}_\ell$) of the Z^0 to charged leptons [20]

$$\Gamma_\ell = \frac{G_\mu M_Z^3}{6\pi\sqrt{2}}\left(\bar{V}_l^{\,2} + \bar{A}_\ell^2\right)\left(1 + \frac{3\alpha}{4\pi}\right) \tag{9}$$

$$A_{FB}^{\ell}(M_Z^2) = 3\frac{\bar{V}_e \bar{A}_e}{\bar{V}_e^{\,2} + \bar{A}_e^2}\frac{\bar{V}_\ell \bar{A}_\ell}{\bar{V}_\ell^{\,2} + \bar{A}_\ell^2} + \Delta A_{FB}^{res} \tag{10}$$

where ΔA_{FB}^{res} is the residual contribution to the asymmetry from weak boxes, the imaginary part of the Z^0 propagator and photon exchange. ΔA_{FB}^{res} is about $+0.002$ with the main contribution coming from the imaginary part of the Z^0 propagator. QED radiative corrections must be applied to obtain predictions for the measured asymmetries.

Alternatively, they can be expressed in terms of an effective weak mixing angle $\sin^2\theta_W^{eff}$ and an effective ρ parameter (ρ_{eff}) via the following relations [20]:

$$\bar{A}_\ell^2 = \tfrac{1}{4}\rho_{eff}, \tag{11}$$

$$\bar{V}_\ell^{\,2} = \tfrac{1}{4}\rho_{eff}\left(1 - 4\sin^2\theta_W^{eff}\right)^2. \tag{12}$$

The cross sections and asymmetries computed using these parameterisations have been compared with the MSM calculations of ref. [27] and found to agree at the level of less than 0.1% [20]. A five-parameter fit to the lineshapes and leptonic forward–backward charge-asymmetries, given as a function of $\sqrt{s}$, yields a measurement of the squared vector and axial-vector couplings of the Z^0 to charged leptons (assuming lepton universality):

$$M_Z = 91.177 \pm 0.010(\text{stat.}) \pm 0.02(E_{cm})\ \text{GeV},$$

$$\Gamma_Z = 2.465 \pm 0.019(\text{stat.}) \pm 0.005(\text{syst.})\ \text{GeV},$$

$$\sigma_0 = 41.84 \pm 0.22(\text{stat.}) \pm 0.39(\text{syst.})\ \text{nb},$$

$$\bar{V}_\ell^{\,2} = 0.0003 \pm 0.0009(\text{stat.}) \pm 0.0002(\text{syst.}),$$

$$\bar{A}_\ell^2 = 0.2508 \pm 0.0024(\text{stat.}) \pm 0.0014(\text{syst.}),$$

$$\chi^2/\text{d.o.f.} = 45/54.$$

Equivalently, this fit gives the following values for the ρ_{eff} parameter and the effective weak mixing angle:

$$\rho_{eff} = 1.003 \pm 0.011,$$

$$\sin^2\theta_W^{eff} = 0.241 \pm 0.009.$$

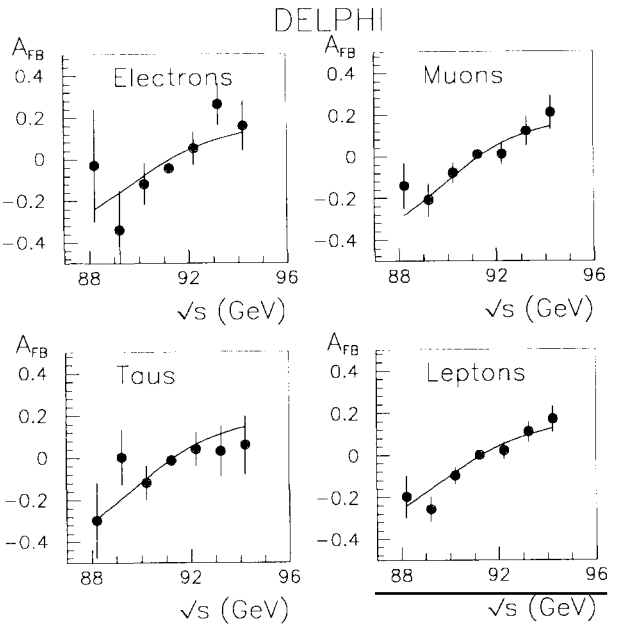

Fig. 16. The forward–backward charge-asymmetries for $e^+e^- \to e^+e^-$ (t-channel subtracted), $e^+e^- \to \mu^+\mu^-$, $e^+e^- \to \tau^+\tau^-$ and $e^+e^- \to l^+l^-$ (flavour-independent analysis, electron t-channel subtracted) as a function of the centre-of-mass energy. The asymmetry data are corrected as described in the text and tables. The curves are the results of a five-parameter fit to the data as described in the text.

The quadratic ambiguity in $\sin^2\theta_W^{\text{eff}}$ contained in the above relation (12) has been resolved by taking the sign of $\overline{V}_l$ to be negative as determined by other experiments [28]. This choice of sign ensures that $\sin^2\theta_W^{\text{eff}}$ is less than 0.25.

The results of the fits to the asymmetries are displayed in fig. 16. In fig. 17 the 68% and 99% confidence level contours in part of the $\overline{V}_\ell$, $\overline{A}_\ell$ plane along with the predictions of the MSM, assuming lepton universality, are shown for the flavour-separated leptonic data, for a range of values of the top quark and Higgs boson masses. It can be seen that the data is in good agreement with the model. The parameter correlation matrix for this fit can be found in appendix A.

An alternative definition of the effective weak mixing angle [28] leads to a different parameterisation of the leptonic partial width:

$$\Gamma_\ell = \frac{\alpha(M_Z^2)M_Z K}{48\sin^2\bar{\theta}_W\cos^2\bar{\theta}_W}\left(1+\left(1-4\sin^2\bar{\theta}_W\right)^2\right)\left(1+\frac{3\alpha}{4\pi}\right), \qquad (13)$$

where K is predicted to be very close to unity in the MSM and depends on the values of the top quark and Higgs boson masses. In particular, the choice $K = 1.0045$ corresponds to $\sin^2\bar{\theta}_W = \sin^2\theta_W^{\overline{\text{MS}}}$, where $\theta_W^{\overline{\text{MS}}}$ is the weak mixing angle defined in the $\overline{\text{MS}}$ renormalisation scheme at $\sqrt{s} = M_Z$. Using this definition and taking into account the variation in K due to the uncertainties in the top-quark

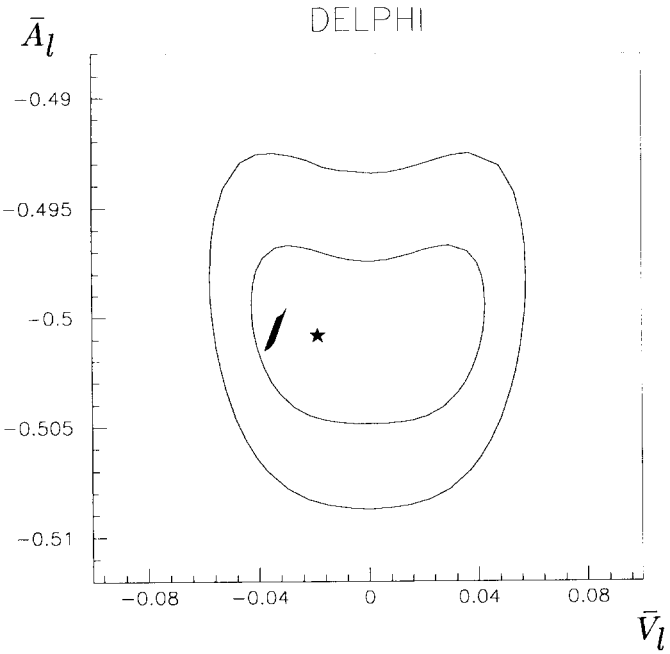

Fig. 17. The 68% and 99% confidence level contours in the $\bar{V}_\ell$, $\bar{A}_\ell$ plane for the five-parameter fit to the $e^+e^- \to e^+e^-$ (t-channel subtracted), $e^+e^- \to \mu^+\mu^-$, $e^+e^- \to \tau^+\tau^-$ and $e^+e^- \to$ hadrons data displayed in fig. 12, fig. 14 and fig. 16. Also shown is the MSM prediction for three massless neutrino species assuming a top-quark mass of 139 ± 38 GeV, a Higgs mass of 300 GeV, allowed to vary from 50 to 1000 GeV, and a value of α_s, of 0.110 ± 0.006.

mass (± 0.0005) and the Higgs-boson mass (± 0.0016), the results of a four-parameter fit to the same data gives

$$\sin^2\theta_W^{\overline{MS}} = 0.2338 \pm 0.0027.$$

The specification of the leptonic couplings in terms of just one parameter leads to a considerably reduced error on the effective weak mixing angle whilst introducing only a rather weak dependence on the MSM through the variation in the value of K.

7.5. FITS TO m_{top} WITHIN THE MINIMAL STANDARD MODEL

The preceding fits indicate that the measured cross sections and asymmetries can be well described by the Improved Born Approximation formulae of ref. [20] and that the derived parameters agree well with the predictions of the MSM. Consequently, the final stage in the analysis of the data is to attempt to derive values for the unknown MSM input parameters (the top quark and Higgs boson masses) using a full MSM fit to the measured cross sections and asymmetries. However, the data is not very sensitive to the Higgs-boson mass and so this type of

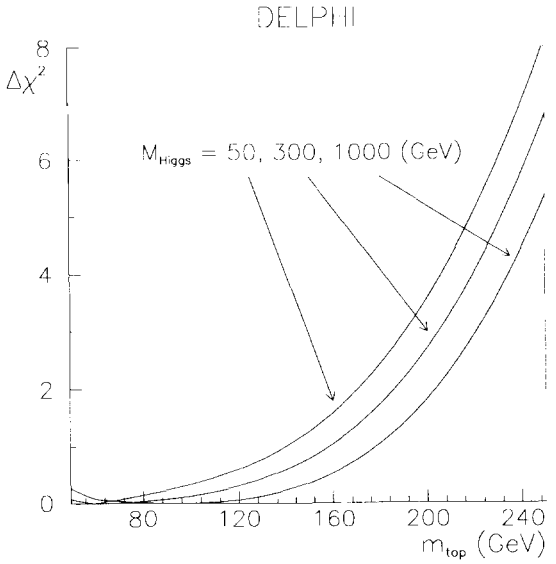

Fig. 18. The $\Delta\chi^2$ as a function of the top-quark mass for the fit described in the text.

analysis is essentially a fit to the top-quark mass. A fit to the lineshapes and asymmetries within the MSM was performed using the the formulae of ref. [20]. For this fit the value $\alpha_s = 0.110 \pm 0.006$ as measured by DELPHI [28] was used as a constraint and the Higgs-boson mass was allowed to vary between 50 GeV and 1000 GeV. The procedure adopted was to fix M_H and allow the parameters M_Z and α_s to vary in order to minimise the χ^2 at each value of m_{top} considered. The whole procedure was repeated for several different values of M_H. The resulting χ^2 curves (expressed as the difference with respect to the absolute χ^2 minimum), shown in fig. 18, give rather shallow minima as a function of m_{top}. However, large values of m_{top} are excluded and the upper limit is derived:

$$m_{top} < 215 \text{ GeV (95\%C.L.)}$$

A lower limit can be obtained for m_{top} from the total width of the Z^0 as described in subsect. 8.2.

8. Interpretation of the results of the fits

The results of the fits described in sect. 7 are discussed in the context of the MSM and, using the measured values of the total and invisible widths, lower limits on the masses of new particles predicted by extensions of or alternatives to the MSM are given. Within the MSM, several observables which are relatively insensitive to variations in the top quark and Higgs masses are examined for possible

TABLE 15
Comparison of fit results using the flavour-dependent and flavour-independent leptonic samples. The predictions of the Minimal Standard Model for these parameters are given in the last column

Parameter	Flavour-dependent	Flavour-independent	MSM
M_Z	91.177 $\pm$0.022 GeV	91.177 $\pm$0.022 GeV	-
Γ_Z	2.465 $\pm$0.020 GeV	2.465 $\pm$0.019 GeV	2.484 $\pm$0.011 GeV
Γ_h	1.726 $\pm$0.019 GeV	1.723 $\pm$0.019 GeV	1.732 $\pm$0.008 GeV
Γ_ℓ	83.4 $\pm$0.8 MeV	83.7 $\pm$0.8 MeV	83.6 $\pm$0.4 MeV
$\overline{A}_8^2 fl$	0.2508 ± 0.0027	0.2515 ± 0.0027	0.2507 ± 0.0009
$\overline{V}_\ell^2$	0.0003 ± 0.0010	0.0002 ± 0.0012	0.0011 ± 0.0002
ρ_{eff}	1.003 $\pm$0.011	1.006 $\pm$0.011	1.003 $\pm$0.004
$\sin^2\theta_W^{eff}$	0.241 $\pm$0.009	$0.243^{+0.007}_{-0.012}$	0.2331 ± 0.0013
$\sin^2\theta_W^{\overline{MS}}$	0.2338 ± 0.0027	0.2330 ± 0.0027	0.2322 ± 0.0012

indications of physics beyond the MSM. The measured value of the invisible width is used to derive the number of light neutrino species in the MSM.

The MSM predictions for the resonance parameters and couplings have been obtained using the formulae of ref. [20] with $M_Z = 91.177 \pm 0.022$ GeV (see sect. 7), $m_{top} = 139 \pm 38$ GeV [32] and $\alpha_s = 0.110 \pm 0.006$ [29], where the errors were assumed to be gaussian, and with a flat distribution for the Higgs-boson mass in the interval 50 to 1000 GeV. The value derived for each parameter is the mean of the probability distribution for the parameter and the error quoted is the r.m.s. of the distribution. It is compared to the data in table 15.

8.1. WITHIN THE MINIMAL STANDARD MODEL

8.1.1. Variables with weak dependence on unknown MSM parameters. There exist within the framework of the MSM several observables which have very little dependence on the two unknown parameters of the model: the top-quark mass and Higgs-boson mass. Consequently the MSM predictions for these observables are rather precise and comparison with their experimentally measured values constitutes an important test of the MSM. Significant deviations from the MSM expectations would be a clear signal for new physics. In particular, there are three such observables which shall be considered here [30]

$$R_Z = \frac{\Gamma_h}{\Gamma_\ell}, \tag{14}$$

$$\sigma_0 = \frac{12\pi\Gamma_e\Gamma_h}{M_Z^2\Gamma_Z^2}, \tag{15}$$

$$T = \frac{3}{59}R_Z - \frac{270}{59}\frac{\Gamma_e}{M_Z\alpha(M_Z)}, \tag{16}$$

R_Z is practically independent of m_{top} due to an almost complete cancellation of m_{top}-dependent terms and the MSM prediction for its value is 20.70 ± 0.04. It also has the experimental advantage of being independent of the luminosity measurement and so can, in principle, be determined very precisely. Unfortunately, σ_0 is directly correlated to the luminosity and so the precision with which it can be measured is limited by the systematic uncertainty on the luminosity. Nevertheless, it exhibits little m_{top} and Higgs-mass dependence and its MSM predicted value is 41.50 ± 0.04 nb. The variable T has been defined in such a way that the only m_{top} dependence is contained in the $Zb\bar{b}$ vertex correction term, which is always negative for m_{top} larger than the limit of about 80 GeV set by $p\bar{p}$ collider data [31]. Thus, in the MSM there is a conservative limit $T < 0.530$.

For the four-parameter fit to the hadronic and leptonic lineshapes, the corresponding values of R_Z, σ_0 and T are

$$R_Z = 20.70 \pm 0.25(\text{stat.}) \pm 0.14(\text{syst.}),$$

$$\sigma_0 = 41.84 \pm 0.22(\text{stat.}) \pm 0.39(\text{syst.}) \text{ nb},$$

$$T = 0.514 \pm 0.016(\text{stat.}) \pm 0.009(\text{syst.}).$$

A substantial fraction (0.21 nb) of the systematic error on σ_0 is due to the theoretical uncertainty on the Bhabha scattering cross section used in the luminosity determination. These measurements are clearly consistent with the expectations of the MSM. The 68% and 99% confidence level contours in the R_Z, σ_0 plane for this fit are shown in figure 19.

8.1.2. Number of light neutrino species. The invisible width, Γ_{inv}, defined as $\Gamma_Z - \Gamma_h - 3\Gamma_\ell$, can be derived from σ_0, R_Z, Γ_ℓ and M_Z with the formula

$$\Gamma_{inv} = \Gamma_\ell \left(\sqrt{\frac{12\pi R_Z}{M_Z^2 \sigma_0}} - R_Z - 3 \right). \tag{17}$$

The corresponding number of light neutrinos species, N_ν, follows by dividing Γ_{inv} by the value of the neutrino partial width, Γ_ν, predicted by the MSM. However, there is less MSM uncertainty for the prediction of the ratio of partial widths. By assuming the MSM prediction for the ratio Γ_ℓ/Γ_ν ($= 0.502 \pm 0.001$), N_ν is obtained from the measured values of R_Z, σ_0 and M_Z. The results are

$$\Gamma_{inv} = 488 \pm 13(\text{stat.}) \pm 11(\text{syst.}) \text{ MeV},$$

$$N_\nu = 2.94 \pm 0.08(\text{stat.}) \pm 0.07(\text{syst.})$$

Alternatively, restricting the analysis to the results of the fit to the hadronic cross-section alone, the values of Γ_ℓ and R_Z were taken from the MSM. Assuming

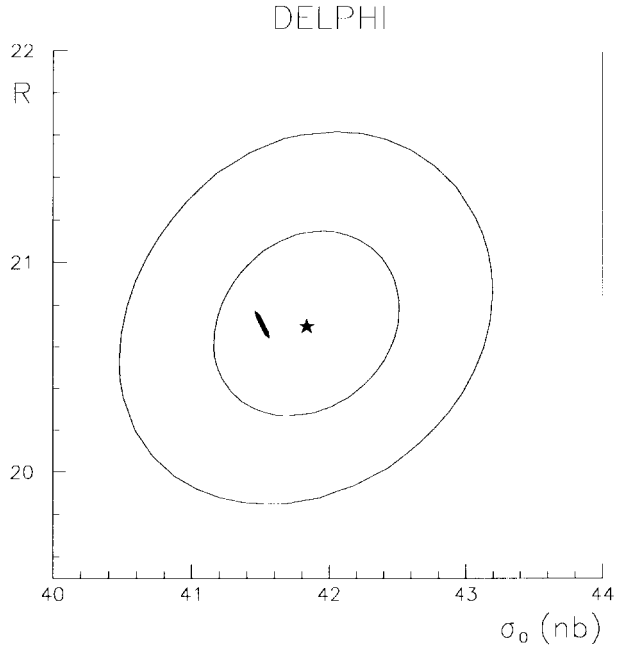

Fig. 19. The 68% and 99% confidence level contours in the R, σ_0 plane for the four-parameter fit to the data displayed in fig. 12 and fig. 14. Also shown is the MSM prediction for three massless neutrino species assuming a top-quark mass of 139 ± 38 GeV, a Higgs mass of 300 GeV, allowed to vary from 50 to 1000 GeV, and a value of α_s of 0.110 ± 0.006.

a top-quark mass of 139 ± 38 GeV [32], a Higgs mass of 300 GeV varying between 50 and 1000 GeV and a strong coupling constant of 0.110 ± 0.006, gives $\Gamma_Z = 83.7 \pm 0.4$ GeV, $R_Z = 20.70 \pm 0.04$ and $\Gamma_\nu = 166.8 \pm 0.6$ MeV. From these values one obtains:

$$\Gamma_{\text{inv}} = 488 \pm 7(\text{stat.}) \pm 12(\text{syst.}) \text{ MeV},$$

$$N_\nu = 2.93 \pm 0.04(\text{stat.}) \pm 0.07(\text{syst.}).$$

The major uncertainty on N_ν comes from the overall normalisation uncertainty of the measured cross sections, which has a 0.5% contribution from the uncertainty on the theoretical Bhabha cross section. The latter uncertainty is transformed into a 0.04 contribution to the systematic error on N_ν mentioned above.

8.2. BEYOND THE MINIMAL STANDARD MODEL

Since there is no evidence for deviations from the predictions of the MSM or for the direct production of new particles, the measured values of Γ_Z and Γ_{inv} were used to derive upper limits on a potential (visible or invisible) partial width due to the Z^0 decaying into a pair of particles predicted by extensions of or

alternatives to the MSM. Using the relationships between the theoretical partial widths of several types of new particles and their masses and couplings to the Z^0 given in appendix B, the upper limits on the partial widths were converted into lower mass bounds for these new particles.

Compared to direct searches, the method based on the widths has the advantage of being sensitive to light, even massless, particles and of being less model-dependent.

Some of the new particles investigated could have a decay length resulting in impact parameters larger than the value of the vertex cuts given in sect. 5. They could also decay into final states with fewer charged particles or less visible energy than the known hadronic Z^0 decays. The efficiency of the selection criteria presented in sect. 5 would therefore be smaller for the new final states than for the known hadronic Z^0 decays. The cross sections would accordingly be underestimated, but by the same relative amount at each collision energy. Thus the measured shape of the resonance would not be biased and the measured value of Γ_Z would reflect properly the contribution of the partial width of the new particle. On the contrary, since Γ_{inv} is inversely proportional to σ_0 (eq. 17), its value would be artificially enhanced.

The upper limits on the new physics contributions to the total and invisible Z^0 width (Γ_Z^{new} and $\Gamma_{\mathrm{inv}}^{\mathrm{new}}$) were computed at the 95% confidence level. Neglecting at first the uncertainty on the widths Γ_Z^{SM} and $\Gamma_{\mathrm{inv}}^{\mathrm{SM}}$ predicted by the MSM, the two limits were obtained by requiring that the measured values Γ_Z^{exp} and $\Gamma_{\mathrm{inv}}^{\mathrm{exp}}$ were 1.65 standard deviations below the theoretical width predicted for the specific particle production investigated:

$$\Gamma_Z^{\mathrm{new}} + \Gamma_Z^{\mathrm{SM}} = \Gamma_Z^{\mathrm{exp}} + 1.65\Delta\Gamma_Z^{\mathrm{exp}}, \tag{18}$$

$$\Gamma_{\mathrm{inv}}^{\mathrm{new}} + \Gamma_{\mathrm{nv}}^{\mathrm{SM}} = \Gamma_{\mathrm{inv}}^{\mathrm{exp}} + 1.65\Delta\Gamma_{\mathrm{inv}}^{\mathrm{exp}}, \tag{19}$$

where $\Delta\Gamma_Z^{\mathrm{exp}}$ and $\Delta\Gamma_{\mathrm{inv}}^{\mathrm{exp}}$ stand respectively for the uncertainties on the measured values of the total and invisible widths.

The above relations do not account for the uncertainties on the predicted widths Γ_Z^{SM} and $\Gamma_{\mathrm{inv}}^{\mathrm{SM}}$. These errors are mainly due to the uncertainty on the masses of the top quark and of the Higgs boson, to the limited knowledge of the strong coupling constant α_s and, to a lesser extent, from the Z^0 mass uncertainty. Whereas the errors on m_{top} and M_Z are gaussian, that on M_{H} and most of that on α_s are not. The two kinds of uncertainties were therefore treated separately. The predicted widths and their gaussian uncertainties were computed assuming $m_{\mathrm{top}} = 139 \pm 38$ GeV [32] and $M_Z = 91.177 \pm 0.022$ GeV. The uncertainties on M_{H} and α_s were taken into account in a most conservative way, viz. as systematic shifts. The values of M_{H} and α_s were chosen to give the smallest predictions for the widths Γ_Z^{SM} and $\Gamma_{\mathrm{inv}}^{\mathrm{SM}}$. To be conservative, α_s was therefore taken equal to 0.098 and M_{H} equal to 1 TeV. The corresponding values of the theoretical widths were

found to be *

$$\Gamma_Z^{SM} = 2472^{+10}_{-8} \text{ MeV},$$

$$\Gamma_{inv}^{SM} = 499.5^{+1.9}_{-1.5} \text{ MeV}.$$

Treating the uncertainties coming from m_{top} and M_Z in the same way as the uncertainties on the experimental widths, the previous relations can be rewritten as follows:

$$\Gamma_Z^{new} + \Gamma_Z^{SM} = \Gamma_Z^{exp} + 1.65\Delta\left(\Gamma_Z^{exp} - \Gamma_Z^{SM}\right), \tag{20}$$

$$\Gamma_{inv}^{new} + \Gamma_{inv}^{SM} = \Gamma_{inv}^{exp} + 1.65\Delta\left(\Gamma_{inv}^{exp} - \Gamma_{inv}^{SM}\right), \tag{21}$$

where $\Delta(\Gamma_Z^{SM} - \Gamma_Z^{exp})$ and $\Delta(\Gamma_{inv}^{SM} - \Gamma_{inv}^{exp})$ are the gaussian uncertainties on the difference between the measured widths and their MSM predictions.

The limits thus obtained are

$$\Gamma_Z^{new} < 28 \text{ MeV},$$

$$\Gamma_{inv}^{new} < 18 \text{ MeV}.$$

Since these upper limits were derived in a fairly conservative way the corresponding confidence level is to be considered higher than 95%. The values of Γ_Z^{new} and Γ_{inv}^{new} were converted into lower bounds on the masses of several new particles, using the relations given in appendix B.

Among the many extensions of and alternatives to the MSM, the effects predicted for some of the most commonly examined are considered here. Besides evaluating limits on particles beyond the MSM, the particular case of the direct production of top-quark pairs was also considered (for that case Γ_Z was computed with $m_{top} = 45$ GeV and was found equal to 2453 MeV).

The different hypothetical new particles considered here can be classified in four categories:

(i) the top-quark;

(ii) a fourth generation of sequential fermions (like Dirac and Majorana neutrinos, left handed charged leptons, a fourth down-type quark) as predicted by extensions of the MSM;

(iii) sneutrinos, sleptons and squarks as predicted by Minimal Supersymmetry (MSSM) and associated bosons and charginos;

(iv) excited charged leptons and quarks as predicted by Composite models (u*, d* and L^{+}*).

The second column of table 16 gives the limits computed as explained above (method I). The third column gives the limits obtained by applying the procedure

* The upper bound on the Higgs mass is not precisely known. In order to illustrate the sensitivity of the MSM predictions to its value the theoretical values were also computed with a Higgs mass of 2 TeV; this reduced the value of Γ_Z^{SM} given above by 3 MeV and that of Γ_{inv}^{SM} by 0.4 MeV.

TABLE 16
Lower mass bounds on new particles in GeV, using the two methods described in the text: method I (column 2) and method II (column 3). The values correspond to a confidence level higher than 95%. Except when indicated as coming from Γ_{inv}, they are derived from Γ_Z. (L + R) refers to mass degenerate left and right symmetric superpartners; LSP is the lightest supersymmetric particle

Particle type	Lower bound (GeV)	
top quark	43	43
b′ quark	45	45
$L^{\pm}$	33	31
L^0_{Dirac}	44	44
L^0_{Dirac} (from Γ_{inv})	45	44
$L^0_{Majorana}$	38	37
$L^0_{Majorana}$ (from Γ_{inv})	40	38
u-type squark (L + R)	39	38
d-type squark (L + R)	40	40
squarks (L + R) (5 flavours)	44	44
sleptons (L + R)	22	18
sneutrino	32	31
LSP sneutrino (from Γ_{inv})	36	33
chargino	44	44
u*	45	44
d*	45	45
$L^{\pm}$*	33	31

advocated by the Particle Data Group [33] (method II) *, excluding the probability of negative values of Γ^{new}. Limits which were found far below those obtained from direct searches by DELPHI were ignored. It is not excluded that some of the lower bounds given in table 16 are actually underestimated because of one major approximation used to derive them: for each single bound, it was assumed that the partial width Γ^{new} was entirely due to the new particle considered. This is true for a new fermion generation if all other particles, apart from the one under investigation, are much heavier than the mass limit obtained. For MSSM the picture is more complicated because of the new gauge and scalar bosons, which also modify the radiative corrections of the Z^0 propagator.

Some of the limits given in table 16 occur in the collision energy range of the lineshape scan. The consequential effects of production thresholds or narrow resonance formation have been neglected in the computation of the limits. However, these effects can most likely be safely ignored as long as the value of the lower mass bound remains below about 44 GeV.

* Instead of treating the theoretical uncertainties like systematic shifts, they were treated as gaussian. For this purpose the shifts in the widths due to these non-gaussian errors were divided by two and combined quadratically with the other uncertainties. That part of the probability distribution corresponding to positive values was then normalized to unity. The limits obtained in this case were $\Gamma_Z^{new} < 33$ MeV and $\Gamma_{inv}^{new} < 27$ MeV.

It should be noted that the region covered by the top-quark mass uncertainty comes from a fit to the radiative corrections to the W^+ and Z^0 propagators. Considering new particles in weak isospin doublets, the allowed region for m_{top} might be significantly altered. However, it remains valid as an effective parameterisation of the radiative corrections, so that the mass limits obtained should not be destroyed by higher-order effects.

9. Summary

A total sample of 150 000 hadronic and leptonic decays of the Z^0 was recorded with the DELPHI detector from August 1989 to August 1990. Subsamples of 125 000 hadronic events and 10 000 leptonic events, collected under good data-taking conditions have been selected, corresponding to an integrated luminosity of 5.88 pb^{-1} for the hadrons and 4.35–4.97 pb^{-1} for the leptons. The hadronic and leptonic lineshapes of the Z^0 boson were measured at 7 different centre-of-mass energies in the vicinity of the resonance peak during 1990, in addition to the measurements made at 10 different centre-of-mass energies in 1989. They have been compared to the line shapes predicted by the Minimal Standard Model and good agreement was observed. The leptonic forward–backward charge-asymmetries were measured with the 1990 data and were used to extract effective couplings of the Z^0 to charged leptons. The energy dependence and magnitude of the asymmetry measurements are also in good agreement with the predictions of the MSM. Our results are also in agreement with other measurements performed at LEP [34].

Both the hadronic and leptonic measurements have been independently cross-checked. In the case of the hadronic cross section, two analyses have been performed, one based mainly on reconstructed charged particle tracks and the other depending on the use of calorimetric information. Each of these analyses gave very consistent results. In the case of the leptonic cross sections and forward–backward charge-asymmetries, there have been analyses in which the leptonic events were separated by flavour and an analysis in which the events were selected without distinguishing the flavour. The results obtained using these two approaches were also very consistent. The results of the fits to the hadronic and leptonic (flavour-separated) data described in sect. 7 are summarized in table 17.

A precise determination (relative error 2×10^{-4}) has been made of the mass of the Z^0 boson, which is one of the fundamental input parameters of the MSM. The number of light neutrino species, derived with a very weak MSM assumption, is

$$N_\nu = 2.94 \pm 0.10.$$

The universality of leptonic couplings to the Z^0 has been confirmed and values for the vector and axial-vector couplings, assuming universality, have been obtained. In the $\overline{\text{MS}}$ renormalisation scheme the effective weak mixing angle at

TABLE 17
Summary of combined fit results to the hadronic and (flavour-separated) leptonic data. The predictions of the Minimal Standard Model for these parameters are given in the last column

parameter	DELPHI	MSM
M_Z	91.177 ± 0.022 GeV	–
Γ_Z	2.465 ± 0.020 GeV	2.484 ± 0.011 GeV
Γ_h	1.726 ± 0.019 GeV	1.732 ± 0.008 GeV
Γ_ℓ	83.4 ± 0.8 MeV	83.6 ± 0.4 MeV
Γ_e	82.4 ± 1.2 MeV	83.7 ± 0.4 MeV
Γ_μ	86.9 ± 2.1 MeV	83.7 ± 0.4 MeV
Γ_τ	82.7 ± 2.4 MeV	83.5 ± 0.4 MeV
$\bar{A}_\ell^2$	0.2508 ± 0.0027	0.2507 ± 0.0009
$\bar{V}_\ell^2$	0.0003 ± 0.0010	0.0011 ± 0.0002
ρ_{eff}	1.003 ± 0.011	1.003 ± 0.004
$\sin^2\theta_W^{\text{eff}}$	0.241 ± 0.009	0.2331 ± 0.0013
$\sin^2\theta_W^{\overline{\text{MS}}}$	0.2338 ± 0.0027	0.2322 ± 0.0012
R_Z	20.70 ± 0.29	20.70 ± 0.04
T	0.514 ± 0.019	< 0.530
σ_0	41.84 ± 0.45 nb	41.50 ± 0.04 nb
Γ_{inv}	488 ± 17 MeV	500 ± 2 MeV
N_ν	2.94 ± 0.10	3
m_{top}	< 215 GeV	–

$\sqrt{s} = M_Z$ has been extracted

$$\sin^2\theta_W^{\overline{\text{MS}}} = 0.2338 \pm 0.0027.$$

Within the framework of the MSM, limits on the top-quark mass have been derived:

$$43 < m_{\text{top}} < 215 \text{ GeV} \quad (95\%\text{C.L.}).$$

Since no sign of physics beyond the MSM was observed, the difference between the measured values of the total and invisible widths and their values predicted by the MSM allows one to determine upper bounds on the partial width due to the production of pairs of new particles predicted by extensions of or alternatives to the MSM. The limit obtained from the total width is 28 MeV and that from the invisible width is 18 MeV. These values correspond to a confidence level higher than 95%. They were used to derive lower bounds on the mass of the top quark, the mass of fermions in a fourth sequential family, of supersymmetric particles and of excited quarks and leptons. Some of these limits improved the values obtained from direct searches.

In conclusion, the analysis of the data taken in 1990 reduced most of the statistical and systematic uncertainties on the line shape parameters determined in 1989 by more than a factor 2. Further improvements are needed for high-precision

tests of the MSM. The large increase in luminosity expected at LEP in the coming years, combined with a better understanding of systematic uncertainties, will allow this aim to be fulfilled.

We are greatly indebted to our technical staff and funding agencies for their support in building the DELPHI detector, and to members of SL division for the excellent performance of the LEP collider.

Appendix A. Parameter correlation matrices

TABLE A.1
Fit to the hadronic and flavour-dependent leptonic cross sections, assuming lepton universality (subsect. 7.3.1)

Parameter	M_Z	Γ_Z	Γ_ℓ	Γ_h
M_Z	1.00	0.12	0.10	0.10
Γ_Z	0.12	1.00	0.63	0.51
Γ_ℓ	0.10	0.63	1.00	0.11
Γ_h	0.10	0.51	0.11	1.00

TABLE A.2
Fit to the hadronic and flavour-dependent leptonic cross sections, not assuming lepton universality (subsect. 7.3.2)

Parameter	M_Z	Γ_Z	Γ_e	Γ_μ	Γ_τ	Γ_h
M_Z	1.00	0.12	0.06	0.05	0.04	0.08
Γ_Z	0.12	1.00	0.45	0.26	0.22	0.37
Γ_e	0.06	0.45	1.00	−0.25	−0.21	−0.43
Γ_μ	0.05	0.26	−0.25	1.00	0.31	0.56
Γ_τ	0.04	0.22	−0.21	0.31	1.00	0.47
Γ_h	0.08	0.37	−0.43	0.56	0.47	1.00

TABLE A.3
Fit to the hadronic and flavour-dependent leptonic cross sections and forward–backward charge asymmetries, assuming lepton universality (subsect. 7.4)

Parameter	M_Z	Γ_Z	σ_0	$\bar{V}_\ell^2$	$\bar{A}_\ell^2$
M_Z	1.00	0.12	0.01	0.07	0.04
Γ_Z	0.12	1.00	−0.32	0.01	0.58
σ_0	0.01	−0.32	1.00	0.00	0.15
$\bar{V}_\ell^2$	0.07	0.01	0.00	1.00	−0.35
$\bar{A}_\ell^2$	0.04	0.58	0.15	−0.35	1.00

Appendix B. Cross section formulae for new particles

The various cross sections given below are normalized to $\sigma_{\nu\bar{\nu}}$. To a good approximation, initial-state radiation is common to all processes and thus does not

affect the normalized cross sections. Final-state radiative corrections are very small and can be neglected in the present context.

QCD corrections for quarks, excited quarks and superpartners are only relevant near threshold where they produce large effects through the Schwinger term [35]. These corrections are used in the exponentiated form [36]

$$K_{\mathrm{QCD}} = \frac{A}{(1 - \mathrm{e}^{-A})},$$

where $A = 4\pi\alpha_s/3\beta$, β being the speed of the pair-produced quarks

$$\beta = \sqrt{(1 - 4m_q^2/M_Z^2)}.$$

At threshold β goes to 0, the correction diverges like $1/\beta$ but the cross section remains finite since the phase space term goes like β.

B.1. PAIR OF FERMIONS

The normalized cross section is given by

$$R_{f\bar{f}} = (K/2)\left[\beta^3 + \left(1 - 4\,|\,Q_f\,|\,\sin^2\theta_{\mathrm{W}}\right)^2 \beta(3 - \beta^2)/2\right],$$

where Q_f is the charge of the fermion and where $K = 1$ for leptons and $K = 3K_{\mathrm{QCD}}$ for quarks. This formula applies to excited quarks or leptons having the same weak isospin as standard fermions.

B.2. MAJORANA NEUTRINOS

$$R_{\mathrm{MM}} = \beta^3$$

B.3. SQUARKS AND SLEPTONS

$$R_{f\tilde{f}} = 2K\beta^3\left(Q_f \sin^2\theta_{\mathrm{W}} - I_3\right)^2$$

where $I_3 = 0$ for $\tilde{f}_{\mathrm{R}}$ and $I_3 = \pm 1/2$ for $\tilde{f}_{\mathrm{L}}$.

B.4. CHARGINOS

One assumes that the chargino behaves like a Higgsino, the superpartner of the Higgs boson. This hypothesis gives the lowest cross section. One has

$$R_{\chi^+\chi^-} = \beta(3 - \beta^2)\left(1 - 2\sin^2\theta_{\mathrm{W}}\right)^2$$

References

[1] DELPHI Collaboration, P. Abreu et al., Phys. Lett. B241 (1990) 435
[2] DELPHI Collaboration, P. Aarnio et al., Phys. Lett. B241 (1990) 425
[3] C. Jarlskog, Orchids to the Standard Model, CERN-TH 5657/90 (1990)
[4] DELPHI Collaboration, P. Aarnio et al., Nucl. Instrum. Methods A303 (1991) 233
[5] G. Barbiellini et al., Atti Accad. Naz. Lincei 44 (1968) 233;
J.F. Crawford et al., Nucl. Instrum. Methods 127 (1975) 173
[6] F.A. Berends, W. Hollik and R. Kleiss, Nucl. Phys. B304 (1988) 712;
M. Böhm, R. Kleiss and W. Hollik, Nucl. Phys. B304 (1988) 687
[7] S. Jadach, E. Richter-Was, B.F.L. Ward and Z. Was, Phys. Lett. B253 (1991) 469
[8] S. Jadach, E. Richter-Was, B.F.L. Ward and Z. Was, Phys. Lett. B260 (1991) 438
[9] W. Beenakker, F.A. Berends and S.C. van der Marck, Nucl. Phys. B355 (1991) 281
[10] J.E. Campagne and R. Zitoun, Z. Phys. C43 (1989) 469; *in* Proc. Brighton Workshop on Radiative corrections, Sussex, July 1989
[11] T. Sjostrand, Comput. Phys. Commun. 39 (1986) 347
T. Sjostrand and M. Bengtsson, Comput. Phys. Commun. 43 (1987) 367, Version 7.2.
[12] F. Kapusta and T. Todorov, private communication
[13] F. Kapusta et al. DELPHI-note 90-42 (1990), unpublished
[14] S. Jadach, B. Ward, Z. Was, R. Stuart and W. Hollik, *in* Z physics at LEP 1, Vol. 3, ed. G. Altarelli et al., CERN 89-08 (1989) p. 69
[15] A. Hoffmann, private communication
[16] V. Hatton et al., LEP absolute energy in 1990, LEP performance note 12 (1990), unpublished
[17] DELPHI Collaboration, DELPHI event generation and detector simulation – User guide, DELPHI note 89-67 (1989), unpublished
[18] F.A. Berends and R. Kleiss, Nucl. Phys. B186 (1981) 22
[19] W.J.P. Beenakker, F.A. Berends and S.C. van der Marck, Nucl. Phys. B349 (1991) 323
[20] D. Bardin et al., Z. Phys. C44 (1989) 493; Comput. Phys. Commun. 59 (1990) 303; Nucl. Phys. B351 (1991) 1;
A.A. Akhundov et al., Nucl. Phys. B276 (1986) 1
[21] F. Aversa, M. Greco, G. Montagna and O. Nicrosini, Phys. Lett. B247 (1990) 93
[22] DELPHI Collaboration, P. Abreu et al., Phys. Lett. B260 (1991) 240
[23] S. Nova et al., Monte Carlo event generator for two-photon physics; DELPHI note 90-35 (1990), unpublished
[24] F.A. Berends, P.H. Daverveldt and R. Kleiss, Phys. Lett. B148 (1984) 489; Comput. Phys. Commun. 40 (1986) 271
[25] G. Altarelli et al., ed., Z physics at LEP 1, Vol. 1, CERN-89/08 (1989) p. 89
[26] A. Borrelli et al., Nucl. Phys. B333 (1990) 357
[27] W. Hollik, Fortschr. Phys. 38 (1990) 165
[28] G. Altarelli, Proc. 1989 Int. Symp. on Lepton and photon interactions at high energies, Stanford University, August 7-12, 1989, ed. M. Riordan (World Scientific, Singapore, 1990) p. 286
[29] DELPHI Collaboration, P. Abreu et al., Phys. Lett. B247 (1990) 167; B252 (1990) 149
[30] G. Girardi, W. Hollik and C. Verzegnassi, Phys. Lett. B240 (1990) 492
[31] CDF Collaboration, F. Abe et al., Phys. Rev. Lett. 64 (1990) 142
[32] F. Dydak, Results from LEP and SLC, CERN-PPE/90-14 (1990)
[33] Particle Data Group, Phys. Lett. B239 (1990) III.35
[34] L3 Collaboration, L3 preprint-28 (February 1991);
OPAL Collaboration, CERN-PPE/91-67 (March 1991);
ALEPH Collaboration, Z. Phys. C48 (1990) 365
[35] J. Schwinger, Particle sources and fields, Vol II (Addison Wesley, Reading, MA, 1973) p. 397
[36] V. Novikov et al. Phys. Rep. 41 (1978) 1